García, M. A., Rickards, J., Cuerno, R., Trejo Luna R., Cañetas Ortega, J., Vega, L. R. de la y Rodríguez Fernández, L. (2017). Surface Morphologies of Ti and Ti-Al-V Bombarded by 1.0-MeV Au + Ions. *Physical Review Applied*, 8 (6), 064027

DOI: 10.1103/PhysRevApplied.8.064027

Surface Morphologies of Ti and Ti-Al-V Bombarded by 1.0-MeV Au^+ Ions

M. A. Garcia,[1] J. Rickards,[1] R. Cuerno,[2,*] R. Trejo-Luna,[1] J. Cañetas-Ortega,[1]
L. R. de la Vega,[3] and L. Rodríguez-Fernández[1]

[1]*Instituto de Física, Universidad Nacional Autónoma de México, Apartado Postal 20-364, 01000 México, Distrito Federal, Mexico*
[2]*Departamento de Matemáticas y Grupo Interdisciplinar de Sistemas Complejos (GISC), Universidad Carlos III de Madrid, Avenida de la Universidad 30, 28911 Leganés, Spain*
[3]*Universidad Autónoma de la Cuidad de México, Avenida la Corona 320 Apartado Postal, 07160 México, Distrito Federal, Mexico*

(Received 12 September 2017; published 26 December 2017)

Ion implantation is known to enhance the mechanical properties of biomaterials such as, e.g., the wear resistance of orthopedic joints. Increasing the surface area of implants may likewise improve their integration with, e.g., bone tissue, which requires surface features with sizes in the micron range. Ion implantation of biocompatible metals has recently been demonstrated to induce surface ripples with wavelengths of a few microns. However, the physical mechanisms controlling the formation and characteristics of these patterns are yet to be understood. We bombard Ti and Ti-6Al-4V surfaces with 1.0-MeV Au^+ ions. Analysis by scanning electron and atomic force microscopies shows the formation of surface ripples with typical dimensions in the micron range, with potential indeed for biomedical applications. Under the present specific experimental conditions, the ripple properties are seen to strongly depend on the fluence of the implanted ions while being weakly dependent on the target material. Moreover, by examining experiments performed for incidence angle values $\theta = 8°$, 23°, 49°, and 67°, we confirm the existence of a threshold incidence angle for (ripple) pattern formation. Surface indentation is also used to study surface features under additional values of θ, agreeing with our single-angle experiments. All properties of the surface structuring process are very similar to those found in the production of surface *nanopatterns* under low-energy ion bombardment of semiconductor targets, in which the stopping power is dominated by nuclear contributions, as in our experiments. We consider a continuum model that combines the effects of various physical processes as originally developed in that context, with parameters that we estimate under a binary-collision approximation. Notably, reasonable agreement with our experimental observations is achieved, even under our high-energy conditions. Accordingly, in our system, ripple formation is determined by mass-redistribution currents reinforced by ion-implantation effects, which compete with an unstable curvature dependence of the sputtering yield.

DOI: 10.1103/PhysRevApplied.8.064027

I. INTRODUCTION

Surfaces with roughness in the nano- to micrometer range have the potential for biomedical applications such as orthopedic implants [1]. This is the case due to the enhanced adherence of associated bone molecules to a metal implant [2–6]. For Ti and its alloys, which are materials with excellent biointegration properties, implantation of a noble gas [7] or gold ions [8] at MeV energies have both demonstrated surface structuring with typical scales in such a desirable range. However, at this time, the physical mechanisms that control the formation of such structures and their characteristics—e.g., how their lateral and vertical dimensions depend on the ion-target combination, the average ion energy, or the incidence angle—are not yet understood. In order to enhance the range of possible bioapplications, it is crucial to identify and understand such type of process. This increased knowledge would open the way to inducing patterns with predesigned morphological properties (e.g., roughness, aspect ratio of surface topographical features, symmetry of their in-plane ordering, etc.) on the material of choice for each specific bioapplication. Moreover, such type of work would bridge the gap between the physics of ion-atom interactions and future technological applications.

In the specific case of the 1.0-MeV Au^+ ion bombardment of Ti and its alloy (Ti-6Al-4V) targets, ripplelike structures do emerge on the surfaces as a result of some self-organization process [8], which are reminiscent of similar behaviors found for ion-beam irradiation at low energies in the (sub-)keV range; see Refs. [9–12] for reviews. For the latter class of systems, surface *nanopatterning* has been attributed to the interplay of surface erosion with the collective behavior of collision cascades within the near-surface region of the material. The phenomenon has a large

*cuerno@math.uc3m.es

degree of universality, featuring similar characteristics independently of the type of substrate (semiconducting, metallic, or insulating) or ion (noble gases, reactive ions).

Even though this type of nanoscale surface structure was initially deemed undesirable [13,14], they are now expected to allow for many different applications from optoelectronics or magnetism to catalysis, or materials biofunctionalization. These applications have fostered the study of surface nanostructuring by ion-beam sputtering (IBS) at low (around 1 keV) to medium (tens of keV) energies, at which the typical scales of the ensuing surface features range from tens to hundreds of nanometers [9–12]. With the goal of controlling the properties of the surface patterns, great effort have been devoted to determine the key physical mechanisms controlling their emergence. Morphological studies have proven quite successful in this regard: for instance, assessing the occurrence of ripple formation or surface smoothing with, e.g., ion incidence angle, allows us to discard one type of mechanism with respect to other, e.g., an unstable geometrical dependence of the sputtering yield with curvature vs surface-confined viscous flow [9–12].

As an important example among the monoelemental targets, silicon is possibly the material which has been studied in greatest detail [15–22] due to its obvious potential for applications, and because it is representative of semiconductors and materials which become similarly amorphous under irradiation by keV ions [12]. Indeed, the present understanding is that sustained ion irradiation induces the formation of an amorphous surface layer that controls the morphological evolution of the system. Under generic conditions on ion species and energy (up to, say, 100 keV, indicating that ion energy loss is mostly due to nuclear stopping) no pattern forms if the angle of incidence of the ions to the surface normal θ is below a threshold value $\theta_c \approx 50°$. At these low-angle conditions, the surface is dominated by mass redistribution [so-called Carter-Vishnyakov (CV) [15,23]] effects induced by the ion beam or, within a mesoscopic description, by viscous flow driven by ion-induced residual stress [21,24–26]. For $\theta > \theta_c$, the differential exposure of surface locations to the ion beam, combined with the incompressibility of the amorphous layer, leads to ripple formation. Actually, the viscous-flow description of the process predicts that the typical ripple wavelength will be roughly proportional to the ion energy, as is seen in many semiconductors [21,25].

For still-larger incidence angles, the thickness of the amorphous layer decreases substantially, and sputtering effects play a role. As pointed out by Bradley and Harper (BH) while they worked on Sigmund's linear cascade approximation in regard to collision cascades [27], the behavior of the sputtering yield with local surface curvature induces roughening since surface minima erode faster than surface maxima: the so-called BH instability. When in competition with smoothing mechanisms such as, e.g., thermal surface diffusion or CV currents, this geometrical effect can also lead to ripple formation, whereby the surface morphology is characterized by a well-defined typical wave number and its associated length scale. We should also note that implantation of nonvolatile or reactive ions has been put forward very recently as a mechanism for ripple formation under low-energy IBS [28,29]. Specifically, ion implantation is seen to act effectively as a negative sputtering yield in such a way that, while it is morphologically stable for incidence angles below a certain threshold value, it has a destabilizing effect along the projection of the beam direction for incidence angles above threshold, akin to the destabilizing effect of mass redistribution or viscous flow for noble-gas ions. Finally, note that it is also possible to induce patterns which differ from simple periodic ripples (e.g., dots, holes, or more-complex ripples) by IBS of Si targets by still other means, e.g., via codeposition or implantation of metallic impurities [30–34]. However, little is known about the possibility of inducing surface patterns at substantially higher ion energies—say, in the 1 MeV range—except for some observations of ripples on silica [35,36].

The previous picture of surface patterning by low-to-medium-energy IBS was developed for semiconductors. In stark contrast, metals do not become amorphous under keV ion irradiation [10,37]. Actually, for low ion fluxes and/or intermediate temperatures (the *diffusive regime*), the surface morphology of metals undergoing IBS is *not* determined by the ion beam. Nevertheless, for large ion fluxes and/or very low or very high temperatures, a so-called erosive regime does exist in which ion irradiation controls the surface morphology [10,37]. In this regime, the behavior is reminiscent of the case of Si at a high incidence angle: the thickness of the surface layer where the material is subject to transport is very small, and erosive BH-type effects seem to dominate [38]. Again, seemingly very little is known about the behavior of metallic targets for high energies in the MeV range.

In this work, we perform a morphological study of Ti and Ti-6Al-4V targets irradiated by 1.0-MeV Au^+ ions. After the realization that surface ripples do arise in such a process [8]—with typical sizes in the micron range that suggest applications to improved tissue-implant biointegration—we conduct a systematic study of the dependence of the ripple formation process with fluence and target material. We explicitly pursue an analogy with the low-energy case in detail in order to investigate the physical nature of the mechanisms controlling the surface pattern-formation process in the MeV range. Specifically, the experimental system we study is characterized by smaller electronic than nuclear contributions to ion stopping, as also occurs under the usual low-to-medium-energy irradiation conditions, which suggests that similar physical processes may be at play. Note that this is comparable to a case of ion irradiation of Si up to 100–120 keV (see Ref. [39] and the references therein), or

of Ge up to 100 keV [40]. Note that, as mentioned above, precisely for the class of targets which are or become amorphous upon low-to-medium-energy irradiation, the typical sizes of the produced surface features scale almost linearly with energy [21,25]. If this result could be extrapolated to high ion energies, it would indicate that the ensuing patterns should have sizes in the micron range, as has been experimentally found [8]. Moreover, at 1 MeV, we assess the occurrence of a threshold value for the incidence angle above which surface ripples develop, again in strong analogy to the case of semiconductors at lower energies. All of these morphological similarities with low-energy ion irradiation may shed light on the physical processes occurring at high energies and could prove helpful in future detailed theoretical investigation of the latter.

The paper is organized as follows. Section II describes our experimental system and procedures. A morphological analysis is presented in Sec. III. The data obtained are considered from a theoretical-modeling perspective in Sec. IV. Section V is devoted to a general discussion of our results. Finally, Sec. VI contains a summary of the main results and our conclusions.

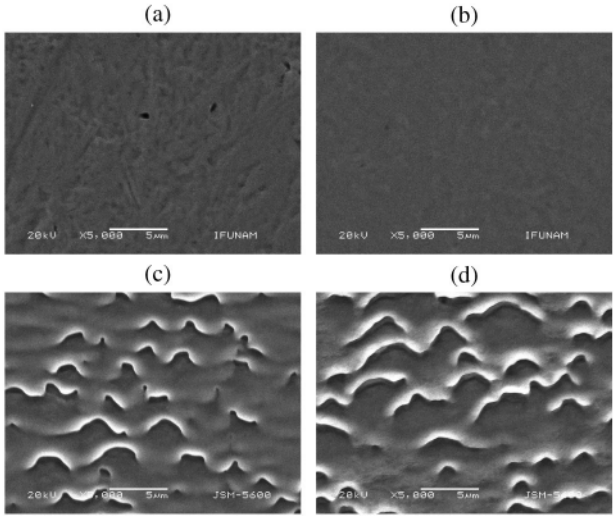

FIG. 1. Scanning-electron-microscopy (SEM) micrographs after $\Phi = 5.0 \times 10^{16}$ ions cm^{-2}, 1.0-MeV Au^+ ion implantation *near-normal incidence* ($\theta = 8°$) for (a) Ti and (b) Ti-6Al-4V, and under *oblique incidence* ($\theta = 45°$) for $\Phi = 6.7 \times 10^{16}$ ions cm^{-2} on (c) Ti and (d) Ti-6Al-4V targets. The ion-beam direction runs from top to bottom in all images.

II. EXPERIMENTS

In this research, Ti and Ti-6Al-4V rods with a 1.0-cm diameter, purchased from Goodfellow Corporation, are cut to a thickness of 3–5 mm and polished to a mirror finish. The manufacturer-quoted purity for Ti is 99.6+%, and the alloy is distributed accordingly by weight: 90% Ti, 6% Al, and 4% V. The polishing procedure consists of grinding paper from P400 to P4000 (FEPA grading), followed by 3.0-, 1.0-, and 0.5-μm diamond compounds and ending with an ultrasonic bath for 30 min in ethyl alcohol. 1.0-MeV Au^+ ions are then implanted in the near surface of Ti and Ti-6Al-4V using a 3 MV tandem Pelletron accelerator (NEC 9SDH-2 Pelletron) located at the Instituto de Física of the Universidad Nacional Autónoma de México (UNAM). Implanted ions reach, on average, a depth of almost half a micron at 45° angle, with a distorted Gaussian distribution leaning toward the surface [8]. Room-temperature experiments are performed, with the temperature increasing up to 150 °C during implantation, as measured with a thermocouple. Vacuum conditions remained at 10^{-7} torr. For this work, a series of experiments is performed; pairs of samples (Ti and Ti-6Al-4V) are implanted for fluences $\Phi = 5.0 \times 10^{16}$ ions cm^{-2}, 1.68×10^{17} ions cm^{-2}, 1.17×10^{17} ions cm^{-2}, 1.33×10^{17} ions cm^{-2}, and 6.7×10^{16} ions cm^{-2}, with a flux of 5.2×10^{12} ions cm^{-2} s^{-1} and at incidence angles $\theta = 8°$, 23°, 45°, 49°, and 67° with respect to the surface normal. Angles of incidence $\theta = 23°$, 49°, and 67° are also investigated by indentation with a Vickers™ microhardness tester before implantation. Angles of incidence on each plane within the indentation are different and depend on the ion-beam direction. Obtained surfaces are subsequently analyzed with electron microscopes (JEOL SEM, model 5600-LV and JEOL SPM, model 4210) revealing the formation of ripples and similar structures. Initial polished surfaces are also characterized by atomic force microscopy (AFM) in tapping mode, displaying an average roughness of 8.24 ± 4.6 nm (22.9 ± 12.5 nm) for the Ti (Ti-6Al-4V) sample, over a (25×25)-μm area. After ion implantation, the surface roughness changes according to ion fluence and angle of incidence.

Ion-implantation experiments carried out for near-normal ($\theta = 8°$) and oblique ($\theta = 45°$) incidence show a clear difference; see Fig. 1 for scanning-electron-microscopy (SEM) images. Both materials, Ti and its alloy Ti-6Al-4V, show rough morphologies for near-normal incidence, but ripples at 45°. These ripples are quite disordered, their ridges showing many interruptions, but they constitute a distinctively different morphology than the near-normal incidence topographies. An oblique incidence angle often correlates with a higher erosion rate of the target material. This angle dependence induces faster evolution of the surface, with the result of an undulated morphology in this case, in contrast to the result for near-normal ion incidence. For the $\theta = 45°$ condition, SEM and optical micrographs for a longer fluence ($\Phi = 4.7 \times 10^{17}$ ions cm^{-2}) are available in Ref. [8]. A comparison with Fig. 1 suggests that the structures shown in the latter merge laterally along sustained irradiation in order to form fully (albeit still disordered) banded structures in the form of faceted ripples. From this point of view, the structures seen in Fig. 1 and their dynamics seem reminiscent of those (etch pits) obtained at early times on the surface of Si targets

by oblique bombardment with suitable, e.g., Ar^+ or Xe^+, (10–40)-keV ions [41–43].

Independent oblique-incidence-angle implantations are also performed in order to understand the possible influence of experimental conditions—fluence, type of target, etc.—on the formation of surface ripples. These conditions are discussed in the next section. Specifically, as mentioned above, a threshold value θ_c exists for the angle of incidence in the case of semiconductor IBS at low to medium energies, such that ripples form only for $\theta > \theta_c$; this is already evident in our case. A critical angle like this signals a loss of stability with respect to surface morphology of some of the physical mechanisms acting in the system. Typically, at lower ion energies, the value of the critical angle θ_c ranges from 45° up to 65°, depending of the ion-target combination [12,21]. An analogous critical angle associated with the implantation of nonvolatile ions also seems to be close to 45°–50° [28,29].

III. SURFACE ANALYSIS

In the case of oblique incidence angles above threshold, the observed pattern shapes can depend on the precise angle of incidence and fluence for each experiment, and they can take different forms even within the time evolution of a single system [27,44,45]. In principle, as in most pattern-forming systems [46], ripple growth at small fluences corresponds to a so-called linear regime, which is the one described, e.g., by the BH or CV models. This time regime is a transient period during which ripples arise as the effect of the amplification or decay of periodic perturbations of a homogeneous configuration of the target height. Under conditions which depend on experimental parameters [10], the amplitude of one of such periodic perturbations is amplified at a maximum rate, its periodicity giving rise to the observed ripple wavelength [15,27]. For longer fluences, additional so-called nonlinear effects take over [44,47], necessarily attenuating the exponential amplitude growth characteristic of the linear regime. Moreover, while ripples have quite a sinusoidal shape during the early-time linear regime, nonlinear effects induce departure of the surface topography from a sinusoidal form, leading eventually into forms which are less up-down symmetric and less smooth, like ridges, facets, defected arrangements, etc. Note, the stochastic nature of ion arrival is an additional source of pattern disorder in the substrate plane by inducing initial amplification of surface disturbances randomly throughout the target [44,47].

A. Fluence dependence of the surface morphology

This subsection describes the surface morphology of ion-implanted Ti and Ti-6Al-4V samples for a varying ion fluence at the fixed incidence angle $\theta = 45°$. Ion implantations for both materials are performed at fluences of $\Phi = 6.5 \times 10^{16}$, 6.7×10^{16}, 1.17×10^{17}, and 4.7×10^{17} ions cm^{-2}. SEM images of these samples are given in Figs. 2 and 3 for Ti and Ti-6Al-4V, respectively. Surface topographies with a higher space resolution, obtained using AFM, are provided in the Supplemental Material (SM) [48]. As a summary of the latter, Fig. 4 displays representative transverse one-dimensional (1D) cuts of these AFM top views for increasing ion fluences, for both the Ti and Ti-6Al-4V targets. Note the large

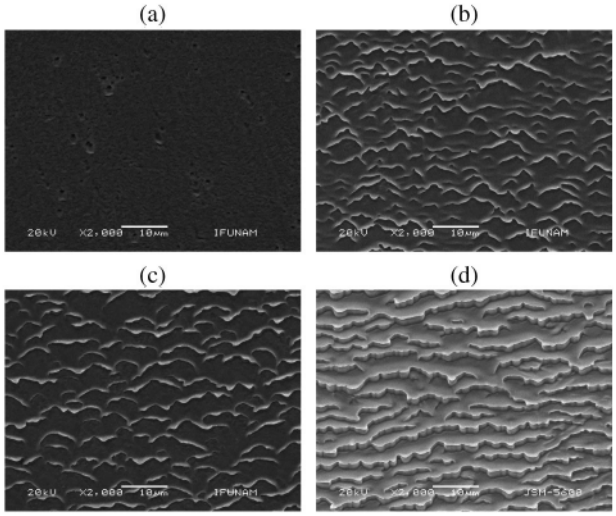

FIG. 2. SEM images of Au^+ ion-sputtered Ti surfaces at 45° for increasing fluences: (a) $\Phi = 6.5 \times 10^{16}$, (b) 6.7×10^{16}, (c) 1.17×10^{17}, and (d) 4.7×10^{17} ions cm^{-2}, at a 2000× magnification. The ion-beam direction runs from top to bottom in all images.

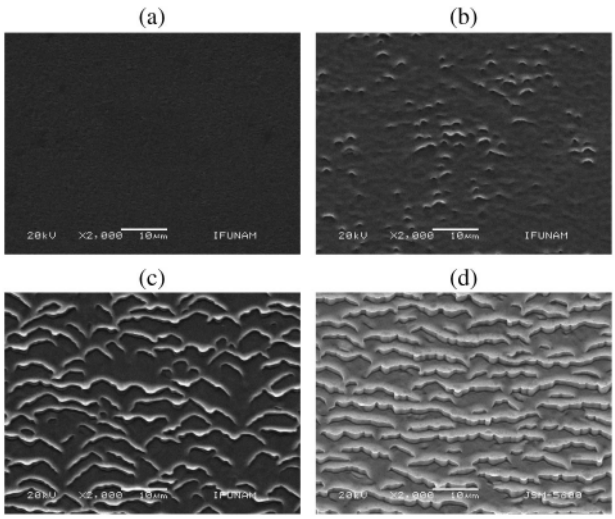

FIG. 3. SEM images of Au^+ ion-sputtered Ti-6Al-4V surfaces at 45° for increasing fluences: (a) $\Phi = 6.5 \times 10^{16}$, (b) 6.7×10^{16}, (c) 1.17×10^{17}, and (d) 4.7×10^{17} ions cm^{-2}, at a 2000× magnification. The ion-beam direction runs from top to bottom in all images.

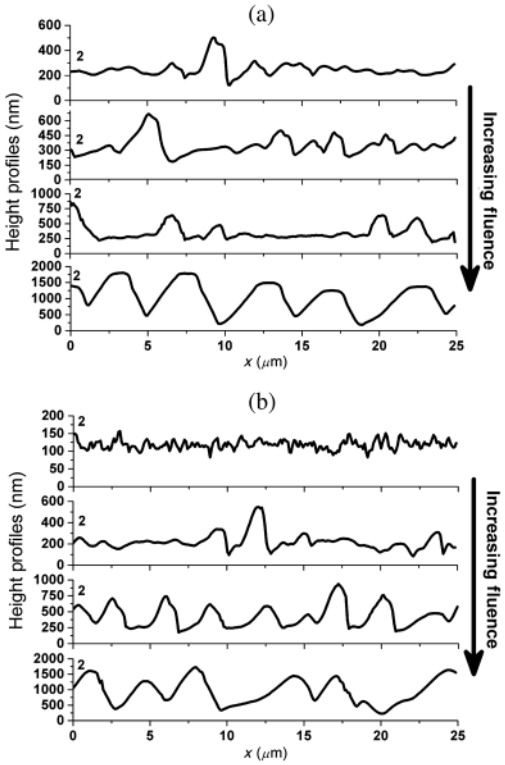

FIG. 4. Transverse height profiles from AFM data in Ref. [48] of ion-implanted Ti (a) and Ti-6Al-4V (b) surfaces at $\theta = 45°$, for increasing fluences $\Phi = 6.5 \times 10^{16}$, 6.7×10^{16}, 1.17×10^{17}, and 4.70×10^{17} ions cm^{-2}, top to bottom. The ion beam direction is from left to right. Note, the horizontal scales are in μm and the vertical scales are in nm.

difference in space resolution for the horizontal and vertical axes employed in this figure, which enhances the surface disturbances. To support our discussion, we carry out statistical analyses of the AFM surface topographies through the corresponding power-spectral-density function, height-height correlation function, and two-dimensional autocorrelation function, as obtained using the GWYDDION software [49,50]; see the SM [48].

Two types of shapes, one nearly symmetric (smaller, with a lateral size of approximately 0.7 μm and a height of about 70 nm) and a second asymmetric (approximately twice as large) one, are already observed in Ti-implanted samples at the smallest fluence, while for Ti-6Al-4V, the surface remains structureless for $\Phi = 6.5 \times 10^{16}$ ions cm^{-2}. The nearly symmetric shapes have similar slopes, while asymmetric shapes differ in their uphill and downhill slopes. For the asymmetric shapes, uphill slopes tend to be smooth, while downhill slopes fall sharply with respect to the ion-beam direction. For an increasing ion fluence, the sawtooth profile becomes more clearly defined for both targets. Still, for the longest fluence, the morphology of Ti-6Al-4V differs somewhat from what is observed in pure titanium: on the alloy surface, structures are less faceted and more symmetric and do not feature flat tops. Although the limited number of fluence values does not allow for a precise determination of the amplitude growth rate, these data suggest a close-to-linear relation between ripple amplitude and implantation dose. At the longest fluence, structures measure approximately 2.5 μm in lateral size and 1 μm in height. In general, asymmetric sawtooth forms arise frequently at low and medium energies due to the geometric shadowing effect induced by the ion beam [12,39,51].

B. Surface morphology dependence with the incidence angle

As mentioned above, up-to-date data for low-to-medium ion energies suggest the case of semiconductor targets as the most similar class of systems to the one we are investigating, in the sense that there is a nonzero threshold angle for ripple formation. This section is devoted to assessing in more detail the dependence of the ripple formation process with θ for our Ti and Ti-6Al-4V targets. Indeed, the results shown in Fig. 1 indicate that, under 1.0-MeV Au^+ irradiation, $0° < \theta_c < 45°$. Furthermore, we observe that there exists an incubation fluence of approximately 6.0×10^{16} cm^{-2} for both materials, below which no ripples form. Again, this is similar to the case for semiconductors at low-to-medium energy [12].

We carry out additional experiments at $\theta = 23°$, 45°, 49°, and 67°. Figures 5 and 6 provide SEM images of the ensuing surfaces for the Ti and Ti-6Al-4V targets, respectively. See the SM [48] for higher-resolution AFM top

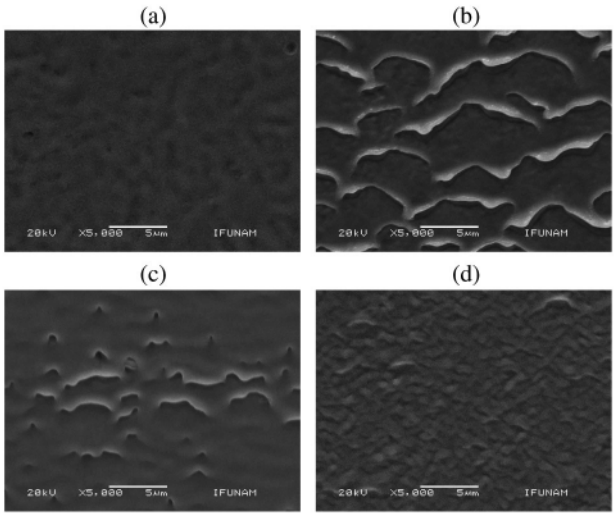

FIG. 5. SEM images of Au^+ ion-sputtered Ti surfaces at a 5000× magnification for (a) $\theta = 23°$, $\Phi = 1.68 \times 10^{17}$ ions cm^{-2}; (b) $\theta = 45°$, $\Phi = 1.17 \times 10^{17}$ ions cm^{-2}; (c) $\theta = 49°$, $\Phi = 1.33 \times 10^{17}$ ions cm^{-2}; and (d) $\theta = 67°$, $\Phi = 6.70 \times 10^{16}$ ions cm^{-2}. The ion-beam direction runs from top to bottom in all images.

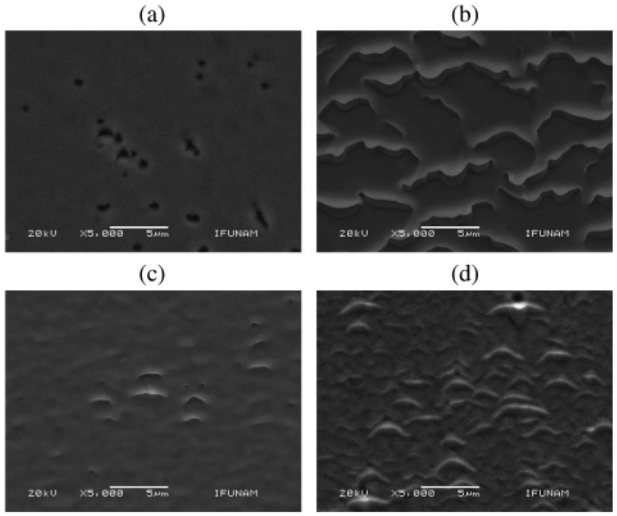

FIG. 6. SEM images of Au^+ ion-sputtered Ti-6Al-4V surfaces at a 5000× magnification for (a) $\theta = 23°$, $\Phi = 1.68 \times 10^{17}$ ions cm^{-2}; (b) $\theta = 45°$, $\Phi = 1.17 \times 10^{17}$ ions cm^{-2}; (c) $\theta = 49°$, $\Phi = 1.33 \times 10^{17}$ ions cm^{-2}; and (d) $\theta = 67°$, $\Phi = 6.70 \times 10^{16}$ ions cm^{-2}. The ion-beam direction runs from top to bottom in all images.

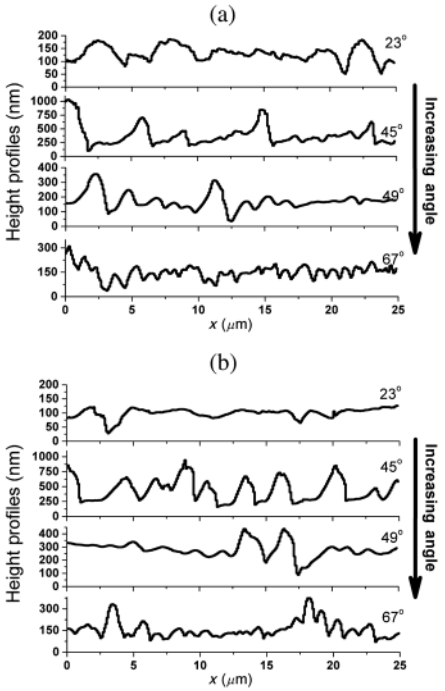

FIG. 7. Transverse height profiles of ion-implanted (a) Ti and (b) Ti-6Al-4V for increasing angles of incidence $\theta = 23°$, 45°, 49°, and 67°, running from top to bottom. Line scans are taken at marked positions of the corresponding AFM top views in the SM [48], all running from top to bottom, along the projection of the ion-beam direction. Note that the horizontal scales are in μm and the vertical scales in nm.

views. The latter are summarized in Fig. 7, which displays representative transverse 1D cuts for increasing incidence angles. Maximum-to-minimum height differences are given in Table I.

Inspection of these figures suggests similarities and differences between the two target materials. At low incidence angles ($\theta = 23°$), the surfaces appear to be rough, with large round shapes for Ti samples, but they are nearly flat for the alloy. Nevertheless, the overall maximum-to-minimum height difference is similar for the two materials; see Table I. Also, in both cases, at higher angles of incidence ($\theta = 45°$), highly disordered surface ripples form, and they are less pronounced and disordered for the still-larger $\theta = 49°$. These surface changes seem to be very similar to those previously found on Si at approximately 20 keV [41–43]. Finally, at more-glancing angles where $\theta = 67°$, the morphology becomes less anisotropic and rough for Ti, and slightly so also for the alloy, although some anisotropy still remains.

Further work regarding the dependence on the angle of incidence is carried out by inducing textures on other surface planes. A microhardness tester (Matsuzawa MHT-2) with a Vickers indenter geometry is utilized to make indentations on Ti and Ti-6Al-4V surfaces. This procedure creates four triangular planes; two opposite pairs of planes form angles of 136° and 22° with respect to the surface normal of the sample (see Fig. 8, left panel). A weight $F_g = 200$ gf (gram force) is applied on the surface to deform it. Under normal indentation conditions, the mark left by the indentation resembles a rhomboidal figure on a flat surface, with a depth proportional to $1/7$ of the diagonal. In the rotated version (a squarelike mark is obtained), if an ion beam at $\theta = 45°$ implants the region in the presence of the marking, angles of 23°, 49°, and 67° with respect to these planes occur (see Fig. 8, right panel). The applied stress on the samples is approximately equal to 2.15 and 3.23 GPa for Ti and Ti-6Al-4V, respectively [52]. The formation of surface structures occurs regardless of the initially applied pressure and depends only on the angle of incidence; compare the generation of surface structures for 67° and 49° with the behavior under $\theta = 23°$ in Fig. 9. This result is reminiscent of the irrelevance of the initial state of disorder in the surface amorphous layer obtained for the low-energy irradiation of Si [53]. Overall, the θ-dependent behavior we find in our indentation experiments agrees largely with the results obtained through single-angle-of-incidence implantations.

Finally, careful inspection of the indentation borders suggests the accumulation of material, the motion of surface ripples in the direction of the ion beam, and the

TABLE I. Maximum-to-minimum height difference (in nm) of implanted surfaces of Ti and Ti-6Al-4V over an area of 625 μm^2.

Material	$\theta = 23°$	$\theta = 45°$	$\theta = 49°$	$\theta = 67°$
Ti	105.0±27.7	354.4±151.1	166.0±39.8	156.7±47.4
Ti-6Al-4V	103.4±16.6	412.9±154.8	290.2±49.4	161.3±45.6

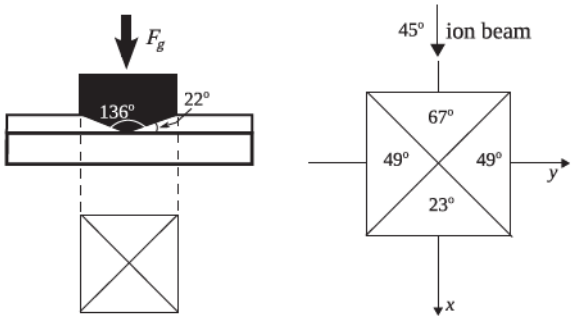

FIG. 8. (Left panel) A pyramidal indenter. (Right panel) The ion-beam direction runs from top to bottom on the x-z plane at an angle of incidence of 45°. The angles shown are those that each face forms with the incident ion-beam direction.

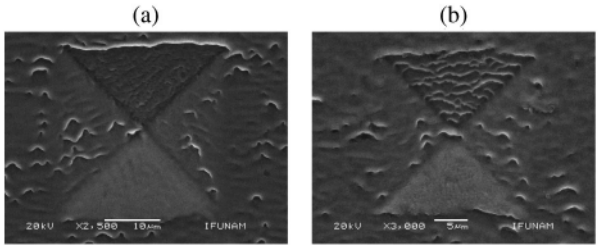

FIG. 9. Square indentations along with ripples for (a) Ti and (b) Ti-6Al-4V surfaces. Ion fluence $\Phi = 6.7 \times 10^{16}$ ions cm^{-2}. The ion-beam direction runs from top to bottom in both images.

stopping at the borders of the indentation. All of these features are reminiscent of ripple in-plane transport as induced viscous flow at the topmost surface layer, as in the low-to-medium-energy case of semiconductor and insulator targets [24,53–55].

IV. MODELING CONSIDERATIONS

The macroscopic time scales associated with surface pattern formation and evolution in IBS experiments make continuum models a natural choice for the theoretical description [56]. This type of framework has been particularly well developed for systems in which the stopping power is dominated by nuclear contributions [57]. Hence, it is quite natural to discuss our results in the context of such continuum models. Indeed, in our experiments, the incubation time for ripple formation is in the range of hours, while, as can be checked by Stopping and Range of Ions in Matter (SRIM) simulations [58], the energy distribution is dominated by nuclear contributions; see the SM [48] for a numerical comparison between the nuclear and electronic stopping powers, where semiempirical models of the sputtering yield [59,60] are considered.

A. Physical mechanisms

For systems which are or which become amorphous under irradiation—like semiconductors at low-to-medium ion energies—a continuum model of ripple formation was developed in the late 1980s based on the dependence of the sputtering yield upon the surface geometry and the angle of incidence, combined with relaxation by thermally activated surface self-diffusion [27]. The model is a partial differential equation for the height of the bombarded target, meant to describe the linear stages of evolution. In this linear model, Bradley and Harper [27] were able to successfully predict the direction and wavelength of surface ripples at high temperatures. While this well-known model captures the essential elements of many experimental observations [10], it fails to predict roughness saturation, an important experimental observation at long time periods. Likewise, given its neglect of mass-redistribution effects [15], the BH models fails to predict the nonzero threshold value for the incidence angle which is observed in most amorphizable materials [12]. Note, however, that these effects seem to be less relevant for metals at low-to-medium ion energies [10,37] since the degree of amorphization is drastically smaller in comparison [61].

Improvements over the original BH model have been put forward that incorporate additional linear and nonlinear mechanisms; see Ref. [56] for an overview. For systems in which a nonzero value of θ_c occurs, CV [15] seminally advocated the role of mass redistribution to counterbalance a morphologically unstable sputtering yield, so $\theta_c \neq 0$. Still, the ensuing original CV prediction of a universal $\theta = 45°$ value has been demonstrated to not be accurate experimentally [21]. Microscopically, this shortcoming originates in the nontrivial competition between erosive and redistributive effects [22,62,63]. Mesoscopically, it correlates with the properties of the space distribution of residual ion-induced stress that is eventually relaxed via viscous flow. In spite of strong approximations such as, e.g., a constant density, the latter view [21] accounts for the variability of the value of θ_c with the ion-target combination and the scaling of the typical ripple wavelength with the average ion energy.

Note that alternative continuum models exist for the implantation of fast heavy ions into amorphous targets. Based on a description of ion-induced thermal spikes [57], viscoelastic shear stress relaxation in the affected regions has been proposed [64] to account for track formation [65] or for anisotropic plastic deformation [66]. Although implications have been extracted for the topography and evolution of the target surface, in the form of surface smoothing, wave formation, and surface roughening [67], we are not aware of predictions concerning the dependence of these properties on, e.g., incidence angle.

Very recently, proposals of an important pattern-forming role for ion implantation were put forward by Bradley and Hofsäss based on a continuum model of self-sputtering [28], on binary-collision-based Monte Carlo simulations, and on a comparison to low-energy experiments for tetrahedral amorphous carbon films under conditions with

a small sputtering yield [22]. The basic idea is that implantation of a substantial number of nonvolatile ions may, by itself, account for surface nanostructuring. This seems to be a natural proposal for our present system: (i) the mechanism has been shown to lead to $\theta_c \neq 0$ [22,28]; (ii) as such, the amorphization rate may be not sufficiently high for metallic targets; and (iii) when nuclear stopping dominates, cascades occur mostly due to binary collisions, rather than thermal spikes. In view of the previous considerations on alternative mechanisms, these facts suggest a possible role for ion implantation in our experiments. Indeed, after a long fluence, e.g., $\Phi = 4.7 \times 10^{17}$ ions cm^{-2}, an equivalent 80-nm-thick film is implanted, where for Au we have taken an atomic volume of 10.2 cm^3/mol. This is a sizable amount of material that may influence surface topography. Moreover, most of the implanted Au remains relatively close to the surface, especially for long time periods. We employ Rutherford backscattering (RBS) to measure the Au concentration as a function of implanted depth for increasing fluences; see Fig. 10. The evolution is similar for Ti and its alloy, the rate being perhaps faster for the former (as seems to occur with the fluence dependence of the surface topography) than for the latter: while the Au concentration peaks within the target for small fluences, the position of this maximum gets closer to the surface for increasing Φ values. Note that these measurements are over large surface regions and may be influenced by retrodispersed ions arriving from diverse origins throughout the large surface probed.

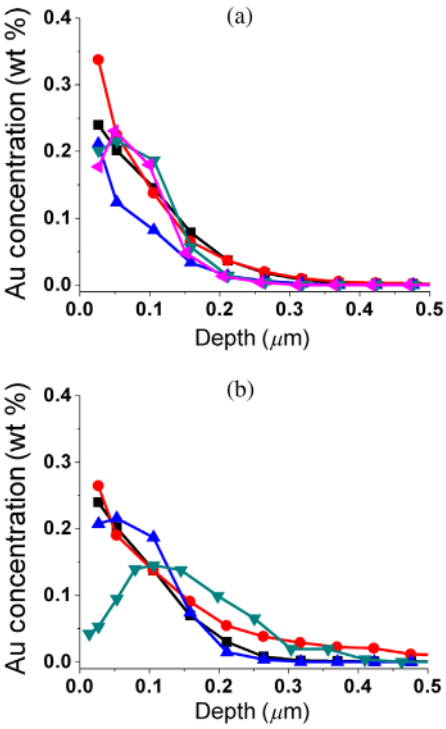

FIG. 10. Au concentration vs implanted depth as measured by RBS, for (a) Ti and (b) Ti-6Al-4V targets irradiated at $\theta = 45°$ and fluences $\Phi = 6.4 \times 10^{16}$ ions cm^{-2} [left-pointing triangle only (a)], 6.5×10^{16} ions cm^{-2} (inverted triangle), 6.7×10^{16} ions cm^{-2} (triangle), 1.17×10^{17} ions cm^{-2} (circle), and 4.7×10^{17} ions cm^{-2} (square). The lines serve as guides for the eye.

B. Continuum model and SRIM simulations

We can estimate the effects on the surface morphology of the competition between sputtering, mass redistribution, and ion implantation. The onset of pattern formation is correctly captured by a linear equation [56]; hence, we consider

$$\frac{1}{J}\frac{\partial h}{\partial t} = C_{11}\frac{\partial^2 h}{\partial x^2} + C_{22}\frac{\partial^2 h}{\partial y^2} - \mathcal{K}\nabla^4 h, \qquad (1)$$

where $h(x, y, t)$ is the height value at time t above point (x, y) on a reference plane, and J is the nominal ion flux. In Eq. (1), we consider only the terms that are relevant to the onset of pattern formation. Ripples form under conditions (e.g., $\theta > \theta_c$) where C_{11} or $C_{22} < 0$, periodic along the direction, x or y, which features the most negative C_{ii} coefficient [10,12]. While different physical mechanisms introduce diverse dependencies of C_{ii} on experimental conditions (e.g., sputtering yield, incidence angle and energy, etc.), the structure of the interface equation (1) is shared by the mechanisms we are discussing. This behavior also applies to $\mathcal{K} > 0$, which collects surface-smoothing contributions from such physical processes.

Given that it is the change of sign of second-order-derivative ("curvature") coefficients, C_{ii}, which signals pattern formation [10,12], and working to linear approximation, we focus on the behavior of these coefficients, for which we consider independent contributions from different processes as

$$C_{ii} = C_{ii}^{\text{sputt}} + C_{ii}^{\text{CV}} + C_{ii}^{\text{impl}}, \qquad i = 1, 2. \qquad (2)$$

The terms on the right-hand side of Eq. (2) correspond, respectively, to sputtering [68,69], mass redistribution [15,17,70], and ion implantation [28]. We will employ certain analytical expressions available in the literature, which relate them to physical parameters, in order to study the onset of pattern formation as a function of the incidence angle. Detailed expressions can be found in the quoted references (see also the Appendix).

Specifically, for sputtering, we consider a recent improvement [68,69] over Sigmund's classic model of energy distribution, which is able to better account for results of molecular-dynamics simulations [71], including predictions on, e.g., maxima of the sputtering yield $Y(\theta)$ for incidence angles $\theta < 90°$. The contribution from mass-redistribution effects to Eq. (2), C_{ii}^{CV}, is modeled by employing the three-dimensional generalization [17] of the original CV formulas, taking into account flux-reduction issues at high incidence angles [70]. To derive an estimate and for computational ease, we leave further

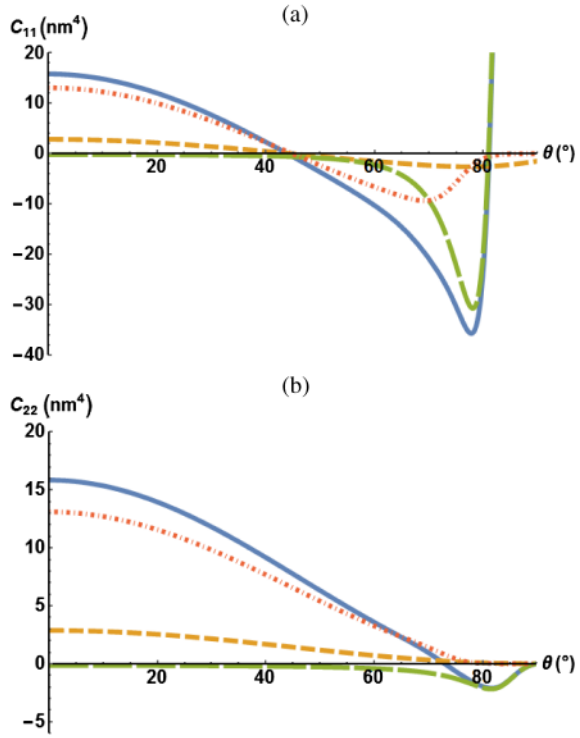

FIG. 11. Dependence of (a) C_{11} and (b) C_{22} in Eq. (2) (solid blue lines) on the angle of incidence, using parameters for Ti as estimated by SRIM; see the Appendix. The specific contributions coming from each physical mechanism are also shown, C_{ii}^{sputt} (long-dashed, green lines), C_{ii}^{CV} (dotted-dashed, red lines), and C_{ii}^{impl} (dashed, brown lines).

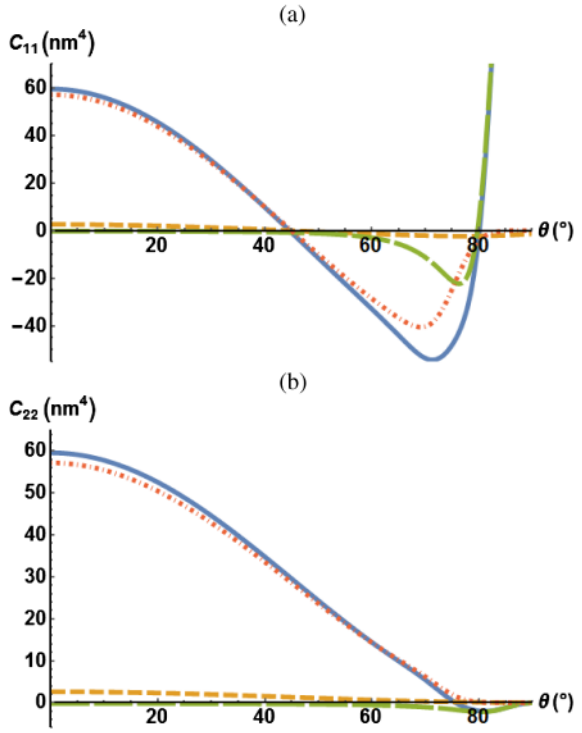

FIG. 12. Dependence of (a) C_{11} and (b) C_{22} in Eq. (2) (solid blue lines) on the angle of incidence for Ti-6Al-4V parameters estimated by SRIM; see the Appendix. The specific contributions coming from each physical mechanism are also shown, C_{ii}^{sputt} (long-dashed, green lines), C_{ii}^{CV} (dotted-dashed, red lines), and C_{ii}^{impl} (dashed, brown lines).

improvements of accuracy [22,62,63] to future studies. Finally, ion implantation contributes to Eq. (2) according to the model in Ref. [28], which is based on the Gaussian-space distribution of implanted ions, readily characterized by binary-collision-based computations. Order-of-magnitude estimates of the resulting contributions to Eq. (2) are $C_{ii}^{\text{sputt}} \approx Y_0 \Omega a_{\text{sputt}}$ [68,69], $C_{ii}^{\text{CV}} \approx \Omega\delta$ [17,70], and $C_{ii}^{\text{impl}} \approx \Omega \alpha_{\text{impl}} \beta_{\text{impl}} a_{\text{impl}}^{-1}$ [28], where Y_0 is the average sputtering yield of a flat surface at normal incidence, Ω is the substrate atomic volume, a_{sputt} (a_{impl}) is the average depth for energy deposition (ion implantation), α_{impl} (β_{impl}) is the corresponding longitudinal (transverse) straggling length, and δ is the average travel distance of the recoil atoms. All of these quantities can be evaluated by SRIM for our experimental conditions; see the Appendix for details. Using the results described there, we obtain $C_{ii}^{\text{sputt}} \approx 9.78\,(9.98)$ nm^4, $C_{ii}^{\text{CV}} \approx 13.11\,(57.18)$ nm^4, and $C_{ii}^{\text{impl}} \approx 0.16\,(0.21)$ nm^4 for Ti (Ti-6Al-4V). These coefficient values already suggest the predominance of mass redistribution for our experimental systems.

Actually, the analytical formulas in Refs. [17,28,68–70] allow us to go further and assess the full behavior of Eq. (2) with incidence angle θ. The results are provided in Fig. 11 (12) for Ti (Ti-6Al-4V), which plots C_{ii} together with the individual contributions from the different physical mechanisms. In spite of quantitative differences in the numerical values of C_{ii}, the qualitative behavior is very similar for Ti and Ti-6Al-4V. Indeed, in both systems, mass redistribution and ion implantation behave similarly (although, in each case, CV currents are numerically larger), with both becoming destabilizing along the x direction for $\theta \gtrsim 45°$ and being unconditionally stabilizing along the y axis. Conversely, and similar to the classic Sigmund description, sputtering is destabilizing along the y direction for all θ values and becomes stabilizing (and numerically substantial) along x for $\theta \gtrsim 80°$. Although not easily appreciated in Figs. 11 and 12 due to the vertical scales employed, $C_{11}^{\text{sputt}} < C_{22}^{\text{sputt}} < 0$ (as classically expected) virtually up to this value of θ. When combining all contributions together, Figs. 11 and 12 predict a critical angle for pattern formation $\theta_c \simeq 45°$, above which ripples appear that are periodic along the x direction. Eventually, for $\theta > \theta_c^* \approx 80°$, the ripple structure rotates and becomes periodic along the y direction.

V. DISCUSSION

The results of our SRIM simulations via the continuum model equation (1) suggest that a competition of mass redistribution, sputtering, and ion implantation drives ripple

formation in our experiments, for both Ti and its alloy. Admittedly, agreement with our experiments is not fully quantitative. Indeed, in view of all the approximations required by the model estimate (in the derivation of the model formulas and in the SRIM estimates of the parameters involved), the 45° value obtained for the critical angle is probably somewhat fortuitous. Also, the value obtained for the second critical angle, at which the ripple orientation rotates, $\theta_c^* \approx 80°$, is likely affected by the approximations made in the sputtering model, which lead to C_{11}^{sputt} peaking (not shown) at roughly 200 nm^4 for $\theta \approx 85°$ for both materials. Likewise, the CV formulas that we employ admit a number of improvements [22,62,63] that may change the numerical value obtained for θ_c^*, perhaps bringing it closer to the 67° value at which our experimental surfaces display less structuring. With respect to the Au ion-implantation profile, note that it evolves with fluence in the experiments (recall Fig. 10), while it is assumed to be time independent in our model above. Nevertheless, the model is meant to describe the pattern-formation mechanism in the (small-fluence) linear regime, during which the experimental implantation profile does conform with the theoretical assumption.

Specifically, Figs. 11 and 12 predict properties of the pattern-formation process that agree with our experiments, including the similarities in the process for Ti and Ti-6Al-4V and the existence of a window of incidence angles $\theta_c < \theta < \theta_c^*$ for the formation of periodic ripples along the x direction. The numerical values obtained for the various contributions to the curvature coefficients indicate a primary role for mass-redistribution effects. Sputtering and ion implantation are comparable in their secondary roles, although the former gains relative importance at high incidence angles, not unlike the case of semiconductor targets at low energies [22,62].

This relevance of mass redistribution indicates that an amorphization process is taking place on the topmost surface layer of the targets, induced by the implantation process. Although we are not yet able to assess such an amorphous layer explicitly in our samples, the existence of an incubation time for pattern formation and the nonzero value of the critical angle that we experimentally assess both agree with this fact. Within a mesoscopic description [21], for $\theta > \theta_c$, pattern formation takes place only provided irradiation has induced enough residual stress in the target, so as to induce ripples in the process of stress relaxation via some form of flow. This property accounts for the incubation time. If the implanted region can be thought of as an incompressible material, then ripples only form for large enough incidence angles θ [21], accounting for the nonzero value of θ_c. While ion implantation reinforces this behavior, a curvature-dependent sputtering yield counteracts it, only overriding it at glancing incidence angles, where mass-redistribution currents (or surface-confined viscous flow) are strongly suppressed by the geometric incidence conditions.

The linear equation (1) describing the formation of ripples predicts, in principle, sinusoidal shapes, while in our experiments, highly disordered ripples are obtained for implantation fluences approximately equal to 10^{17} ions cm^{-2}, with sawtoothlike profiles which are nonsinusoidal. Detailed analyses of the equations of motion relating surface ripples suggest that nonlinear terms are important factors in the long-fluence behavior [44,45,47,72–74]. Specifically, after a crossover time, the nonlinear terms lead to a stabilization of the linear instability [45,75], entering a period dominated by coarsening and/or kinetic roughening of surface structures, which may ultimately lead to a steady state. Ripples remaining during nonlinear behavior are typically nonsinusoidal; hence, it is natural to expect our large fluence surfaces to be within such a dynamical regime.

Our work is performed in the high-energy regime, where the formation of ripples is largely unknown. These experiments are comparison to most of the work found in the literature, which focuses on low energies due to the accessibility and applicability of the available theories [9,10,12]. Since ion damage depends on energy, low-energy implantation is desired for near-surface penetration depths. Surface modifications for the semiconductor industry commonly utilize nanometer-sized components requiring low-energy ions. In the case of our work, Au implantation is much deeper, peaking at around 40 nm within the target for an angle of incidence of 45° [8]. The formation of surface ripples with a mean wavelength on the order of microns ($\lambda \approx 3\ \mu\mathrm{m}$) opens an alternative area of the materials science, with a particular potential for biological applications.

Note that a comparison with low-to-medium-energy experiments still requires a mention of additional aspects—specifically, the type of substrate and of ions. With respect to the first item, we have to further remark that metallic targets are known not to become amorphous under low-to-medium ion bombardment, even within the erosive regime [37]. Furthermore, diffusion and thermally activated relaxation mechanisms play a larger role in the pattern formation on these substrates [38,61]. The formation of surface structures on Ti and Ti-6Al-4V may presumably be subject to similar mechanisms, although the fact that $\theta_c \neq 0$ suggests that they may be less relevant at high energies.

Furthermore, for lower ion energies and monoelemental targets, a sufficiently high concentration of metallic contaminants [19,32,33,76] or the use of metallic ions [34] is known, at times, to play a key role in triggering pattern formation under conditions for which no structure would otherwise form. This behavior is seen, for example, in normal-incidence experiments on semiconductors, where metallic impurities generate a surface instability. Meanwhile, for the case of alloys, ripple formation may emerge as a result of the interplay between differential

sputtering and atomic segregation [77–81]. In the work of Baur and Hormes [82], Au implantation of Ti-6Al-4V substrates with energies in the keV range leads to the intermetallic compound $AuTi_3$. The potential relevance of this compound formation remains to be assessed. However, at least for low-to-medium ion energies, alloy formation and impurity deposition seem to be associated with $\theta_c = 0°$, which again contrasts with our observations.

As mentioned in the Introduction, our experiments are strongly motivated by the potential medical uses of ion-implanted metallic samples since surface structures with roughnesses in a wide range of scales from nanometers to microns offer prospects in orthopedic implant applications [1]. Specifically, Ti and its alloys are known to deliver a high strength-to-weight ratio, increasing longevity in hip and knee replacements [2]. In our case, surface modification by ion implantation with noble ions supports this possibility. Although surface structures obtained through ion irradiation do not automatically guarantee osseointegration, surface chemical post-treatments may assist with the procedure [4].

Numerous studies have focused on the osseointegration mechanism of the metallic implant with the bone tissue [3–7]. The osseointegration of Ti-based biomaterials enables the adherence of proteins and thus the migration of bone cells onto the metal-bone interface. The use of ion implantation along with a post-treatment hydroxyapatite (HA) coating may become an effective method of realizing a biomechanical surface. Moreover, ion-implanted HA-coated Ti-6Al-4V substrates have demonstrated improvement with respect to wear resistance or fatigue properties [4].

Braceras *et al.* [7] performed WST-1 [83] assessments of hFOB 1.19 cells on ion-implanted Ti surfaces, displaying early growth and proliferation. Their tests were performed off of the ATCC recommendation for culture cells. We can speculate that our experimental roughness values are in a suitable range for bone tissue [1,7], which is a couple hundred nanometers, possibly enhancing the adhesion, growth, and proliferation of bone cells.

From a general point of view, while the formation of surface structures is a rather general feature of ion irradiation of materials, their description still lacks a general theory. For technological applications, the dependence of the characteristics of the surface morphology on the materials and on other experimental parameters is significant; hence, the identification of the main physical mechanisms driving the formation of the surface patterns becomes critical. We present advances in the understanding of pattern formation under high-energy bombardment by exploiting the relations with many features of the process at lower ion energies.

VI. CONCLUSIONS

This work explores the formation of surface structures by ion implantation at 1 MeV of energy under different experimental conditions. We demonstrate the occurrence of surface morphological behavior that has been previously assessed at low and medium energies. Specifically, 1.0-MeV Au^+ ion implantation of Ti and Ti-6Al-4V at oblique incidence angles is performed. The formation of surface structures is observed to depend on experimental conditions. For $\theta = 45°$ and a fluence of approximately 6.0×10^{16} ions cm^{-2}, surface ripples begin to form. Micrometer-sized structures are obtained at an increasing ion fluence. The existence of a nonzero critical angle of incidence for ripple formation is akin to that observed at low and medium energies for semiconducting materials. Other surface structures are obtained after ion implantations at 23°, 49°, and 67° angles. These results for oblique-incidence-angle implantations are largely reproduced using Vickers indentations. Both materials behave similarly, despite the enhanced initial surface stress.

Numerical comparison with continuum models developed for low-energy conditions in which nuclear stopping is also predominant allow to identify mass-redistribution effects as the main physical mechanism driving ripple formation in our system. This process cooperates with ion implantation and competes with a curvature-dependent sputtering yield. Nevertheless, other processes need to be considered in the future, such as the formation of compounds with a heterogeneous response under implantation. Our work may thus open alternative areas of study, with a potential for improving the predictive power of current continuum theories of surface structuring under ion bombardment. We note that, to date, no theory has successfully explained the behavior observed at high energies when nuclear stopping is dominant. More elaborate models are expected to describe our experiments, which describe the amorphization of the near-surface region and/or composition-related effects more accurately.

With respect to biomedical applications, as discussed above, the adherence of associated bone molecules on the metal implant is expected to play an important role for osseointegration. It would be interesting to, e.g., compare the performance of our (previously HA-coated) Ti vs Ti-6Al-4V targets with respect to the actual cell growth and proliferation. This comparison would provide a specific practical instance to assess the way in which the surface roughness of orthopedic implants can be controlled via suitable ion-implantation procedures.

ACKNOWLEDGMENTS

The authors wish to acknowledge the technical assistance of M. Galindo, K. López, F. Jaimes, M. Escobar, J. G. Morales, and L. Lartundo-Rojas, and the discussions with M. Castro, R. Gago, A. Redondo-Cubero, J. Muñoz-García, and L. Vázquez. This work was financially supported by Dirección General de Asuntos del Personal Académico-UNAM under Contracts No. Programa de Apoyo a Proyectos de Investigación e Innovación

Tecnológica IN110116 and No. IN111717, and by CONACYT under Contract No. 222485. L. R. d. l. V. is supported by the Programa de Estancias Sabáticas Nacionales del Consejo Nacional de Ciencia y Tecnología (CONACyT). R. C. acknowledges the kind hospitality and support of the Instituto de Física at UNAM while part of this work was being carried out, as well as partial support from Ministerio de Economía y Competitividad/Fondo Europeo de Desarrollo Regional (Spain/European Union) through Grants No. FIS2012-38866-C05-01 and No. FIS2015-66020-C2-1-P.

APPENDIX: SRIM ESTIMATES OF PARAMETERS APPEARING IN THE CONTINUUM EQUATIONS (1) AND (2)

1. (Modified) Sigmund model of sputtering

We estimate the contribution of sputtering to Eqs. (1) and (2) in the main text by evaluating the coefficients C_{ii}^{sputt} for $i = x, y$, as estimated within the improved Sigmund model of energy deposition [69], which agrees better with Monte Carlo simulations than the classic Sigmund model [27]. The analytical derivations performed in that reference require the use of an also improved so-called crater formalism [68]. The parameters appearing in the final formulas of Ref. [69] which we are employing are as follows: the average energy deposition depth a_{sputt}, the longitudinal (α_{sputt}) and transverse (β_{sputt}) straggling lengths, the average sputtering yield of a flat surface at normal incidence Y_0, the substrate atomic volume Ω, and the apparent incidence angle $\psi = \rho\theta$, where $1 < \rho < 2$ is a model constant that can be estimated from the fact [69] that the sputtering yield has a maximum at $\pi/(2\rho)$; specifically, we take $\rho = 90/85$ for both materials; see the representative SRIM results for the yield as a function of θ in the SM [48]. We use numerical values for these quantities either from tables ($\Omega_{\text{Ti}} = 0.018$ nm^3 and $\Omega_{\text{Ti6Al4V}} = 0.016$ nm^3) or from our SRIM simulations following Ref. [70]; see Table II.

As an illustration, Fig. 13 shows the distribution of recoil end positions after irradiation of Ti and Ti-6Al-4V by ten-thousand 1-MeV Au ions under normal incidence, together with Gaussian fits employed to extract the parameter values provided in Table II, as obtained by SRIM.

2. Ion implantation

We estimate the contribution of ion implantation to Eqs. (1) and (2) by evaluating the coefficients C_{ii}^{impl} for $i = x, y$, as estimated within the continuum model of ion (self-)implantation put forward in Ref. [28]. The analytical derivations performed in that reference also require the use of the improved crater formalism described in Ref. [68]. The parameters which enter the final formulas of Ref. [28] which we are employing are as follows: the substrate atomic volume Ω provided in the first section of this appendix, the average implantation depth, a_{impl}, and the longitudinal (α_{impl}) and transverse (β_{impl}) straggling lengths for the ion implantation. We use numerical values for these quantities, which are obtained from our SRIM simulations following the indications in Ref. [70] and are provided in Table III.

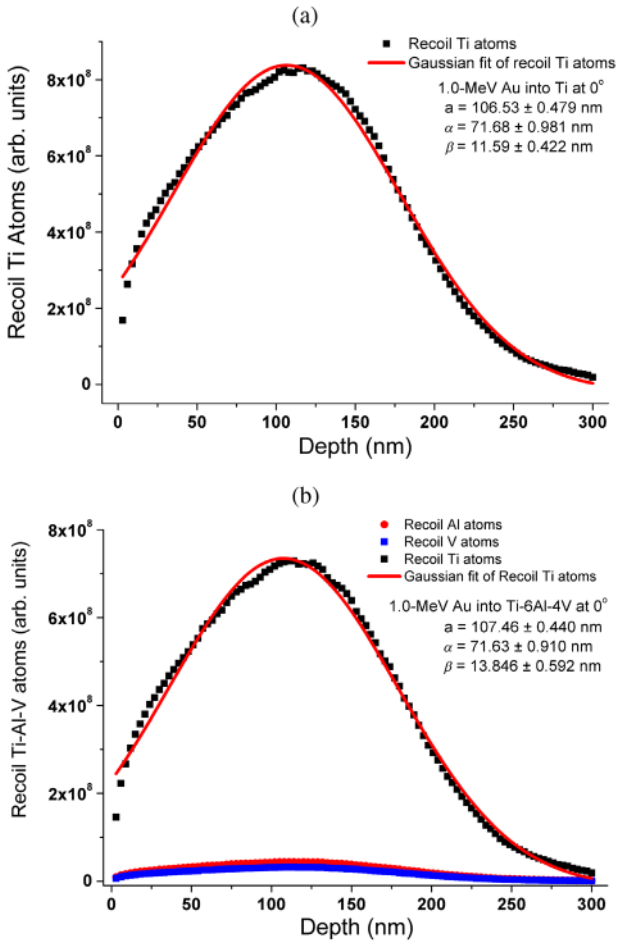

FIG. 13. Distribution of recoil end positions for 1-MeV Au ions implanted on (a) Ti and (b) Ti-6Al-4V at $\theta = 0°$, as calculated by SRIM for 10^4 recoils. The lines represent Gaussian fits.

TABLE II. Parameter values for the sputtering contribution C_{ii}^{sputt} to C_{ii} in Eq. (2).

Material	a_{sputt} (nm)	α_{sputt} (nm)	β_{sputt} (nm)	Y_0 (atom/ion)
Ti	106.5	71.7	11.6	5.1
Ti-6Al-4V	107.5	71.6	13.8	5.8

TABLE III. Parameter values for the contribution C_{ii}^{impl} from ion implantation in Eq. (2).

Material	a_{impl} (nm)	α_{impl} (nm)	β_{impl} (nm)
Ti	160.2	44.6	31.5
Ti-6Al-4V	163.8	44.5	31.9

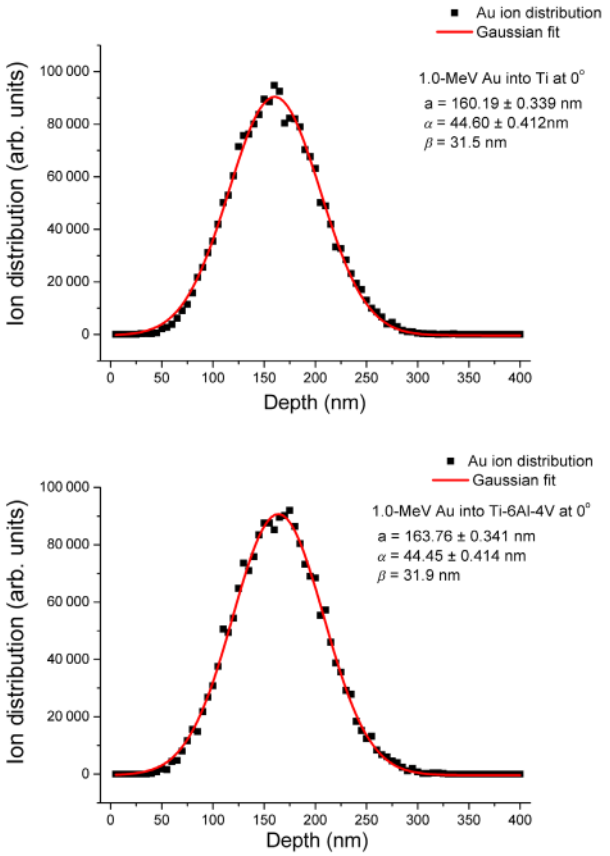

FIG. 14. Space distribution of the final positions for 10^4 (1-MeV) Au ions implanted on Ti (top panel) and Ti-6Al-4V (bottom panel) at $\theta = 0°$, as calculated by SRIM. The lines represent Gaussian fits.

As an illustration, Fig. 14 shows the space distribution of the final positions of ten-thousand 1-MeV Au ions implanted on Ti and Ti-6Al-4V under normal incidence, together with Gaussian fits employed to extract the parameter values provided in Table III, as obtained by SRIM.

3. Mass redistribution

We finally estimate the contribution of mass-redistribution currents to Eqs. (1) and (2) by evaluating the coefficients C_{ii}^{CV} for $i = x, y$, as obtained within the three-dimensional generalization [17] of the original Carter-Vishnyakov [15] model, similarly to Ref. [70]. Specifically, we employ the formulas for C_{ii}^{CV}, with $i = x, y$, which was used in Ref. [17], with a correction factor $f_{\mathrm{corr}}(\theta)$ analogous to the one appearing in Ref. [70], and which arises due to the decrease of the average travel distance of recoil atoms (δ) with increasing incidence angle. Employing the formulas in Ref. [70], our SRIM data (three 10^5-ion runs for each material) lead to the values quoted in Table IV. Here, d_R (d_V) denotes the mean depth of recoils (vacancies), and N_D is the total number of knockon events with energy transfer above the displacement energy, so $\delta = N_D(d_R - d_V)$ [70].

TABLE IV. Parameter values for the contribution C_{ii}^{CV} from the mass redistribution in Eq. (2).

Material	d_R (nm)	d_V (nm)	N_D (1/ion)	δ (nm/ion)
Ti	107.58	107.522	13 494	728.6
Ti-6Al-4V	109.1	108.8	13 140	3574.1

[1] K. Grandfield, Bone, implants, and their interfaces, Phys. Today **68**, No. 4, 40 (2015).
[2] J. B. Park and J. D. Bronzino, *Biomaterials: Principles and Applications* (CRC Press, Boca Raton, 2000).
[3] H. J. Rack and J. I. Qazi, Titanium alloys for biomedical applications, Mater. Sci. Eng. C **26**, 1269 (2006).
[4] T. R. Rautray, R. Narayanan, and K.-H. Kim, Ion implantation of titanium based biomaterials, Prog. Mater. Sci. **56**, 1137 (2011).
[5] N. I. Riedel, J. D. Williams, and K. C. Popat, Ion beam etching titanium for enhanced osteoblast response, J. Mater. Sci. **46**, 6087 (2011).
[6] J. Sommereld, R. Ritcher, R. Neipelt, S. Kosan, T. F. Keller, K. D. Jandt, and C. Ronning, Protein adsorption on nanoscaled, rippled TiO_2 and Si surfaces, Biointerphases **7**, 55 (2012).
[7] I. Braceras, C. Vera, A. Ayerdi-Izquierdo, R. Muñoz, J. Lorenzo, N. Alvarez, and M.A de Maeztu, Ion implantation induced nanotechnology on titanium and bone cell adhesion, Appl. Surf. Sci. **310**, 24 (2014).
[8] M. A. Garcia, J. Rickards, R. Trejo-Luna, J. Cañetas-Ortega, and L. Rodríguez-Fernández, Changes in the surface morphology induced by 1.0-MeV Au ion bombardment of Ti and Ti-6Al-4V, Surf. Interface Anal. **46**, 314 (2014).
[9] G. Carter, The physics and applications of ion beam erosion, J. Phys. D **34**, R1 (2001).
[10] W. L. Chan and E. Chason, Making waves: Kinetic processes controlling surface evolution during low energy sputtering, J. Appl. Phys. **101**, 121301 (2007).
[11] J. Muñoz-García, L. Vázquez, R. Cuerno, J. A. Sánchez-García, M. Castro, and R. Gago, in *Toward Functional Nanomaterials*, edited by Z. M. Wang (Springer, New York, 2009).
[12] J. Muñoz-García, L. Vázquez, M. Castro, R. Gago, A. Redondo-Cubero, A. Moreno-Barrado, and R. Cuerno, Self-organized nanopatterning of silicon surfaces by ion beam sputtering, Mater. Sci. Eng. R **86**, 1 (2014).
[13] R. L. Cunningham, P. Haymann, C. Lecomte, W. J. Moore, and J. J. Trillat, Etching of surfaces with 8-keV argon ions, J. Appl. Phys. **31**, 839 (1960).
[14] M. Navez, C. Sella, and D. Chaperot, Electron microscopy—Investigation of ionic bombardment of glass, C.R. Hebd. Seances Acad. Sci. **254**, 240 (1962).
[15] G. Carter and V. Vishnyakov, Roughening and ripple instabilities on ion-bombarded Si, Phys. Rev. B **54**, 17647 (1996).
[16] C. S. Madi, E. Anzenberg, K. F. Ludwig, Jr., and M. J. Aziz, Mass Redistribution Causes the Structural Richness of Ion-Irradiated Surfaces, Phys. Rev. Lett. **106**, 066101 (2011).
[17] E. Anzenberg, C. S. Madi, M. J. Aziz, and K. F. Ludwig, Jr., Time-resolved measurements of nanoscale surface pattern

formation kinetics in two dimensions on ion-irradiated Si, Phys. Rev. B **84**, 214108 (2011).
[18] M. Castro, R. Gago, L. Vázquez, J. Muñoz-García, and R. Cuerno, Stress-induced solid flow drives surface nanopattering of silicon by ion-beam irradiation, Phys. Rev. B **86**, 214107 (2012).
[19] M. Engler, S. Macko, F. Frost, and T. Michely, Evolution of ion beam induced patterns on Si(001), Phys. Rev. B **89**, 245412 (2014).
[20] S. K. Garg, D. P. Datta, M. Kumar, D. Kanjilal, and T. Som, 60 keV Ar^+-ion induced pattern formation on Si surface: Roles of sputter erosion and atomic redistribution, Appl. Surf. Sci. **310**, 147 (2014).
[21] A. Moreno-Barrado, M. Castro, R. Gago, L. Vázquez, J. Muñoz-García, A. Redondo-Cubero, B. Galiana, C. Ballesteros, and R. Cuerno, Nonuniversality due to inhomogeneneous stress in semiconductor surface nanopatterning by low-energy ion-beam irradiation, Phys. Rev. B **91**, 155303 (2015).
[22] H. Hofsäss, O. Bobes, and K. Zhang, Argon ion beam induced surface pattern formation on Si, J. Appl. Phys. **119**, 035302 (2016).
[23] S. A. Norris, J. Samela, L. Bukonte, M. Backman, F. Djurabekova, K. Nordlund, C. S. Madi, M. P. Brenner, and M. J. Aziz, Molecular dynamics of single-particle impacts predicts phase diagrams for large scale pattern formation, Nat. Commun. **2**, 276 (2011).
[24] C. C. Umbach, R. L. Headrick, and K.-C. Chang, Spontaneous Nanoscale Corrugation of Ion-Eroded SiO_2: The Role of Ion-Irradiation-Enhanced Viscous Flow, Phys. Rev. Lett. **87**, 246104 (2001).
[25] M. Castro and R. Cuerno, Hydrodynamic approach to surface pattern formation by ion beams, Appl. Surf. Sci. **258**, 4171 (2012).
[26] S. A. Norris, Stress-induced patterns in ion-irradiated silicon: Model based on anisotropic plastic flow, Phys. Rev. B **86**, 235405 (2012).
[27] R. M. Bradley and J. M. E. Harper, Theory of ripple topography induced by ion bombardment, J. Vac. Sci. Technol. A **6**, 2390 (1988).
[28] R. M. Bradley and H. Hofsäss, Nanoscale patterns produced by self-sputtering of solid surfaces: The effect of ion implantation, J. Appl. Phys. **120**, 074302 (2016).
[29] H. Hofsäss, K. Zhang, and O. Bobes, Self-organized surface ripple pattern formation by ion implantation, J. Appl. Phys. **120**, 135308 (2016).
[30] R. Gago, L. Vázquez, R. Cuerno, M. Varela, C. Ballesteros, and J. M. Albella, Production of ordered silicon nanocrystals by low-energy ion sputtering, Appl. Phys. Lett. **78**, 3316 (2001).
[31] B. Ziberi, F. Frost, M. Tartz, H. Neumann, and B. Rauschenbach, Ripple rotation, pattern transitions, and long range ordered dots on silicon by ion beam erosion, Appl. Phys. Lett. **92**, 063102 (2008).
[32] S. Macko, F. Frost, M. Engler, D. Hirsch, T. Höche, J. Grenzer, and T. Michely, Phenomenoloy of iron-assisted ion beam pattern formation on Si(001), New J. Phys. **13**, 073017 (2011).
[33] A. Redondo-Cubero, R. Gago, F. J. Palomares, A. Mücklich, M. Vinnichenko, and L. Vázquez, Nanopatterning dynamics on Si(100) during oblique 40-keV Ar^+ erosion with metal codeposition: Morphological and compositional correlation, Phys. Rev. B **86**, 085436 (2012).
[34] S. A. Mollick, D. Ghose, P. D. Shipman, and R. M. Bradley, Anomalous patterns and nearly defect-free ripples produced by bombarding silicon and germanium with a beam of gold ions, Appl. Phys. Lett. **104**, 043103 (2014).
[35] P. Santhana Raman, K. G. M. Nair, M. Kamruddin, A. K. Tyagi, A. Rath, P. V. Satyam, B. K. Panigrahi, and V. Ravichandran, MeV Au^{2+} ions induced surface patterning in silica, Appl. Surf. Sci. **258**, 4156 (2012).
[36] S. K. Srivastava, K. Ganesan, P. Gangopadhyay, B. K. Panigrahi, K. G. M. Nair, and A. K. Tyagi, High energy ion irradiation induced surface patterning on a $Si0_2$ glass substrate, Nucl. Instrum. Methods Phys. Res., Sect. B **338**, 89 (2014).
[37] U. Valbusa, C. Boragno, and F. Buatier de Mongeot, Nanostructuring surfaces by ion sputtering, J. Phys. Condens. Matter **14**, 8153 (2002).
[38] D. Ghose, Ion beam sputtering induced nanostructuring of polycrystalline metal films, J. Phys. Condens. Matter **21**, 224001 (2009).
[39] T. K. Chini, D. P. Datta, and S. R. Bhattacharyya, Ripple formation on silicon by medium energy ion bombardment, J. Phys. Condens. Matter **21**, 224004 (2009).
[40] D. P. Datta, S. K. Garg, T. Basu, B. Satpati, H. Hofsäss, D. Kanjilal, and T. Som, Temporal evolution of Ge surface topography under keV ion irradiation: Combined effects of curvature-dependent sputter erosion and atomic redistribution, Appl. Surf. Sci. **360**, 131 (2016).
[41] G. Carter, M. J. Nobes, C. Cave, and N. Al-Qadi, Ripple production induced by oblique incidence ion bombardement of Si, Vacuum **45**, 71 (1994).
[42] G. Carter, V. Vishnyakov, Yu. V. Martynenko, and M. J. Nobes, The effects of ion species and target temperature on topography development on ion bombarded Si, J. Appl. Phys. **78**, 3559 (1995).
[43] G. Carter and V. Vishnyakov, Ne^+ and Ar^+ ion bombardment-induced topography on Si, Surf. Interface Anal. **23**, 514 (1995).
[44] R. Cuerno and A.-L. Barabási, Dynamic Scaling of Ion-Sputtered Surfaces, Phys. Rev. Lett. **74**, 4746 (1995).
[45] S. Park, B. Kahng, H. Jeong, and A.-L. Barabási, Dynamics of Ripple Formation in Sputter Erosion: Nonlinear Phenomena, Phys. Rev. Lett. **83**, 3486 (1999).
[46] M. Cross and H. Greenside, *Pattern Formation and Dynamics in Nonequilibrium Systems* (Cambridge University Press, Cambridge, England, 2009).
[47] M. A. Makeev, R. Cuerno, and A.-L. Barabási, Morphology of ion-sputtered surfaces, Nucl. Instrum. Methods Phys. Res., Sect. B **197**, 185 (2002).
[48] See Supplemental Material at http://link.aps.org/supplemental/10.1103/PhysRevApplied.8.064027 for AFM top and transverse views, 1D power-spectral-density and 2D autocorrelation function analyses, and additional SEM micrographs and SRIM results for the sputtering yield and stopping power.
[49] D. Nečas and P. Klapetek, Gwyddion: An open-source software for SPM data analysis, Central Eur. J. Phys. **10**, 181 (2012).

[50] M. Raposo, Q. Ferreira, and P. A. Ribeiro, in *Modern Research and Educational Topics in Microscopy*, edited by A. Méndez-Vilas and J. Díaz, Microscopy Series (Formatex, Badajoz, Spain, 2007), Vol. 1, p. 758.
[51] G. Carter, The effects of surface ripples on sputtering erosion rates and secondary ion emission yields, J. Appl. Phys. **85**, 455 (1999).
[52] R. Trejo-Luna, L. R. De la Vega, J. Rickards, C. Falcony, and M. Jergel, 9 MeV Au ion implantation into Ti and Ti-6Al-4V, J. Mater. Sci. **36**, 503 (2001).
[53] A. Moreno-Barrado, M. Castro, J. Muñoz-García, and R. Cuerno, Stress vs sputtering effects in the propagation of surface ripples produced by ion-beam sputtering, Nucl. Instrum. Methods Phys. Res., Sect. B **365**, 13 (2015).
[54] P. F. A. Alkemade, Propulsion of Ripples on Glass by Ion Bombardment, Phys. Rev. Lett. **96**, 107602 (2006).
[55] D. Kramczynski, B. Reuscher, and H. Gnaser, Wavelength-dependent ripple propagation on ion-irradiated prepatterned surfaces driven by viscous flow corroborates two-field continuum model, Phys. Rev. B **89**, 205422 (2014).
[56] R. Cuerno, M. Castro, J. Muñoz-García, R. Gago, and L. Vázquez, Nanoscale pattern formation at surfaces under ion-beam sputtering: A perspective from continuum models, Nucl. Instrum. Methods Phys. Res., Sect. B **269**, 894 (2011).
[57] M. Nastasi, J. W. Mayer, and J. K. Hirvonen, *Ion-solid Interactions: Fundamentals and Applications* (Cambridge University Press, Cambridge, England, 1996).
[58] J. F. Ziegler, M. D. Ziegler, and J. P. Biersack, SRIM—The Stopping and Range of Ions in Matter (2010), Nucl. Instrum. Methods Phys. Res., Sect. B **268**, 1818 (2010).
[59] N. Matsunami, Y. Yamamura, N. Itikawa, Y. Kazumata, S. Miyagawa, K. Morita, R. Shimizu, and H. Tawara, Energy dependence of the ion-induced sputtering yields of monatomic solids, At. Data Nucl. Data Tables **31**, 1 (1984).
[60] Y. Yamamura and H. Tawara, Energy dependence of ion-induced sputtering yields from monatomic solids at normal incidence, At. Data Nucl. Data Tables **62**, 149 (1996).
[61] J. Renedo, R. Cuerno, M. Castro, and J. Muñoz-García, Symmetry of surface nanopatterns induced by ion-beam sputtering: Role of anisotropic surface diffusion, Phys. Rev. B **93**, 155424 (2016).
[62] H. Hofsäss, Surface instability and pattern formation by ion-induced erosion and mass redistribution, Appl. Phys. A **114**, 401 (2014).
[63] H. Hofsäss, Model for roughening and ripple instability due to ion-induced mass redistribution [Addendum to H. Hofsäss, Appl. Phys. A **114**, 401 (2014)], Appl. Phys. A **119**, 687 (2015).
[64] H. Trinkaus and A. I. Ryazanov, Viscoelastic Model for the Plastic Flow of Amorphous Solids under Energetic Ion Bombardment, Phys. Rev. Lett. **74**, 5072 (1995).
[65] H. Trinkaus, Dynamics of viscoelastic flow in ion tracks: Origin of plastic deformation of amorphous materials, Nucl. Instrum. Methods Phys. Res., Sect. B **146**, 204 (1998).
[66] A. Gutzmann, S. Klaumünzer, and P. Meier, Ion-Beam-Induced Surface Instability of Glassy $Fe_{40}Ni_{40}B_{20}$, Phys. Rev. Lett. **74**, 2256 (1995).
[67] A. Gutzmann and S. Klaumünzer, Shape instability of amorphous materials during high-energy bombardment, Nucl. Instrum. Methods Phys. Res., Sect. B **127–128**, 12 (1997).
[68] M. P. Harrison and R. M. Bradley, Crater function approach to ion-induced nanoscale pattern formation: Craters for flat surfaces are insufficient, Phys. Rev. B **89**, 245401 (2014).
[69] R. M. Bradley and H. Hofsäss, A modification to the Sigmund model of ion sputtering, J. Appl. Phys. **116**, 234304 (2014).
[70] O. Bobes, K. Zhang, and H. Hofsäss, Ion beam induced surface patterns due to mass redistribution and curvature-dependent sputtering, Phys. Rev. B **86**, 235414 (2012).
[71] M. Z. Hossain, J. B. Freund, and H. T. Johnson, Ion impact energy distribution and sputtering of Si and Ge, J. Appl. Phys. **111**, 103513 (2012).
[72] M. Castro, R. Cuerno, L. Vázquez, and R. Gago, Self-Organized Ordering of Nanostructures Produced by Ion-Beam Sputtering, Phys. Rev. Lett. **94**, 016102 (2005).
[73] J. Muñoz-García, M. Castro, and R. Cuerno, Nonlinear Ripple Dynamics on Amorphous Surfaces Patterned by Ion Beam Sputtering, Phys. Rev. Lett. **96**, 086101 (2006).
[74] D. A. Pearson and R. M. Bradley, Theory of terraced topographies produced by oblique-incidence ion bombardment of solid surfaces, J. Phys. Condens. Matter **27**, 015010 (2015).
[75] A. Keller, M. Nicoli, S. Facsko, and R. Cuerno, Dynamic effects induced by renormalization in anisotropic pattern forming systems, Phys. Rev. E **84**, 015202(R) (2011).
[76] R. Gago, L. Vázquez, O. Plantevin, T. H. Metzger, J. Muñoz-García, R. Cuerno, and M. Castro, Order enhacement and coarsening of self-organized silicon nanodot patterns induced by ion-beam sputtering, Appl. Phys. Lett. **89**, 233101 (2006).
[77] V. B. Shenoy, W. L. Chan, and E. Chason, Compositional Modulated Ripples Induced by Sputtering of Alloy Surfaces, Phys. Rev. Lett. **98**, 256101 (2007).
[78] R. M. Bradley and P. D. Shipman, Spontaneous Pattern Formation Induced by Ion Bombardment of Binary Compounds, Phys. Rev. Lett. **105**, 145501 (2010).
[79] M. S. Bharathi, H. Ramanarayan, and Y. W. Zhang, Pattern formation and nonlinear evolution in alloy surfaces by ion-beam sputtering, Appl. Phys. Lett. **99**, 083103 (2011).
[80] R. M. Bradley, Nanoscale patterns produced by ion erosion of a solid with codeposition of impurities: The crucial effect of compound formation, Phys. Rev. B **87**, 205408 (2013).
[81] F. C. Motta, P. D. Shipman, and R. M. Bradley, Theory of nanoscale pattern formation produced by oblique-incidence ion bombardment of binary compounds, Phys. Rev. B **90**, 085428 (2014).
[82] K. Baur and J. Hormes, The formation of intermetallic compounds in ion implanted aluminum and Ti6Al4V observed by x-ray absorption spectroscopy, Surf. Sci. **436**, 141 (1999).
[83] WST-1 stands for 4-[3-(4-iodophenyl)-2-(4-nitrophenyl)-2H-5-tetrazolio]-1,3-benzene disulfonate.

Supplemental Material for "Surface Morphologies of 1.0-MeV Au^+ ion Bombardment of Ti and Ti-6Al-4V"

M.A. Garcia, J. Rickards, R. Cuerno, R. Trejo-Luna,
J. Cañetas-Ortega, L.R. de la Vega, and L. Rodríguez-Fernández

I. SURFACE BEHAVIOR WITH FLUENCE, TI

Figure S1 a) shows small structures with a lateral size ≈ 0.7 μm and height 60 nm and a few larger structures at ≈ 2.5 μm and height 200 nm. In Figure S1 b), both shapes appear again, with an increasing number of larger shapes. Small structures have a lateral size ≈ 0.7 μm and height 80 nm; on the other hand, larger structures have a lateral size ≈ 2 μm and height 300 nm. Two or more asymmetric figures appear to merge laterally to form a longer chain-like structure. In Figure S1 c) asymmetric shapes begin to populate the surface, with lateral size ≈ 1.5 μm and height 500 nm. A decrease in number of nearly symmetric shapes occurs at this fluence. In Figure S1 d) asymmetric structures fill the surface and previously observed smaller symmetric shapes are absent. The lateral size of these large asymmetric structures is ≈ 3 μm with an average height of ≈ 1 μm. Saw-tooth like profiles with flat tops are obtained at this high fluence. These estimates are corroborated by the analysis of the Power Spectral Density Functions (PSDF) provided in Fig. S3.

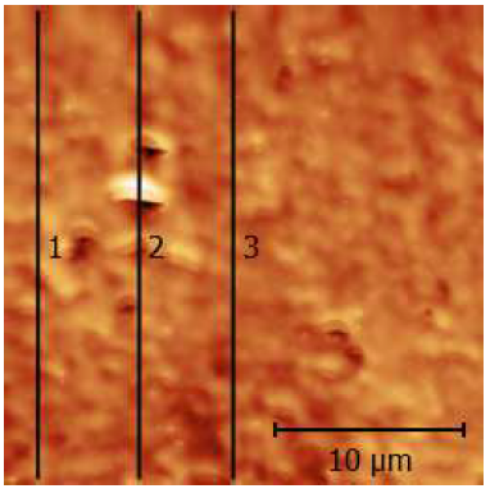

(a) $\Phi = 6.5 \times 10^{16}$ ions cm^{-2}

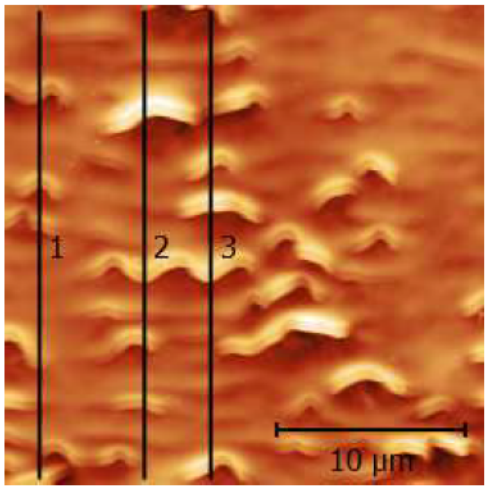

(b) $\Phi = 6.7 \times 10^{16}$ ions cm^{-2}

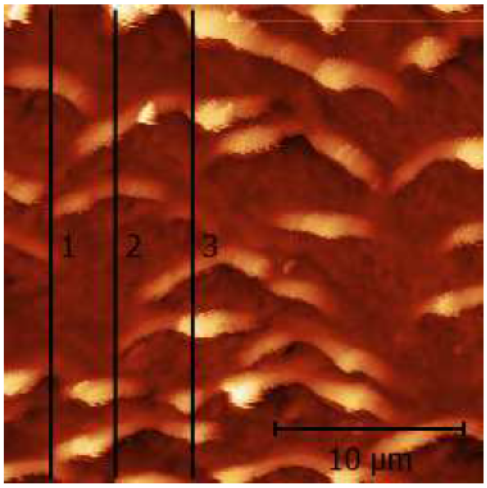

(c) $\Phi = 1.17 \times 10^{17}$ ions cm^{-2}

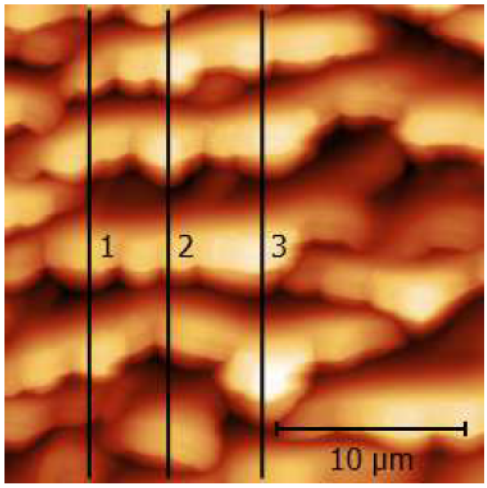

(d) $\Phi = 4.70 \times 10^{17}$ ions cm^{-2}

FIG. S1: AFM micrograph measurements of Ti-sputtered surfaces over 25 μm×25 μm at 45° incidence angle. The ion beam direction is from top to bottom on all images. The ion fluences are indicated in the legends. The numbered vertical solid lines on each top-view indicate the location of the corresponding line profiles shown in Fig. S2.

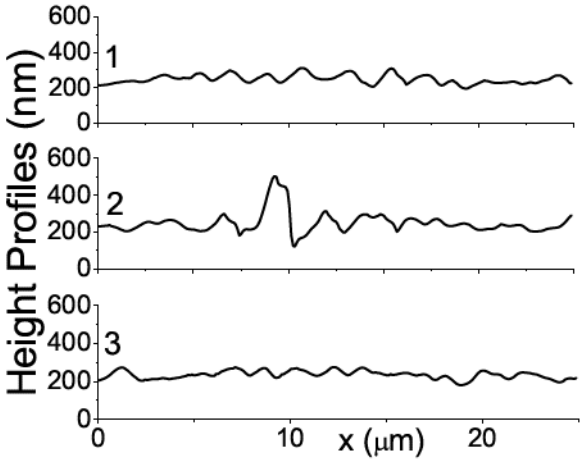

(a) $\Phi = 6.5 \times 10^{16}$ ions cm^{-2}

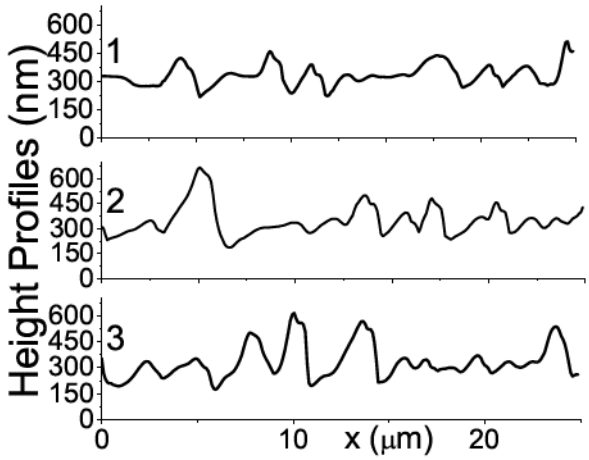

(b) $\Phi = 6.7 \times 10^{16}$ ions cm^{-2}

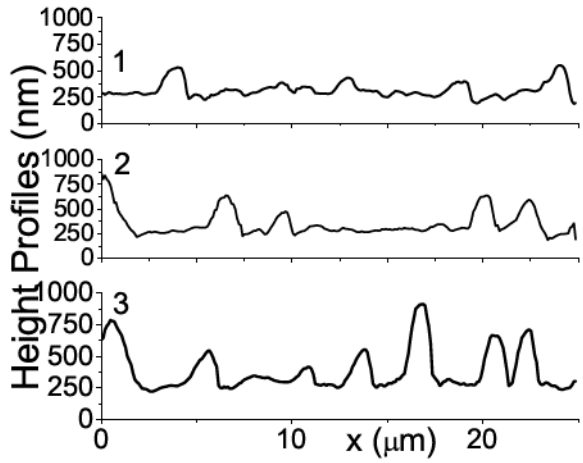

(c) $\Phi = 1.17 \times 10^{17}$ ions cm^{-2}

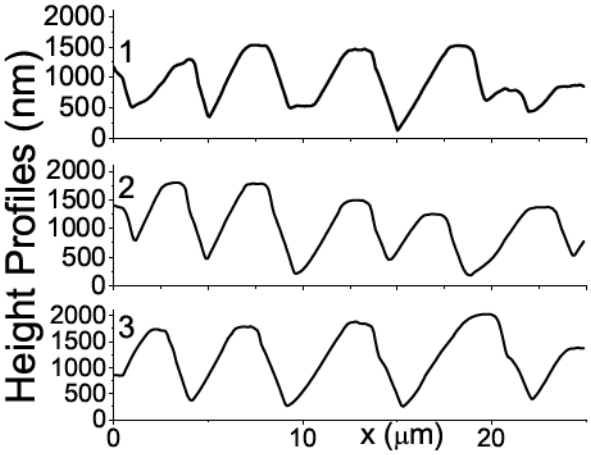

(d) $\Phi = 4.70 \times 10^{17}$ ions cm^{-2}

FIG. S2: Height profile scans of ion implanted titanium surfaces at $\theta = 45°$ corresponding to the top views shown in Fig. S1. The ion beam direction is from left to right.

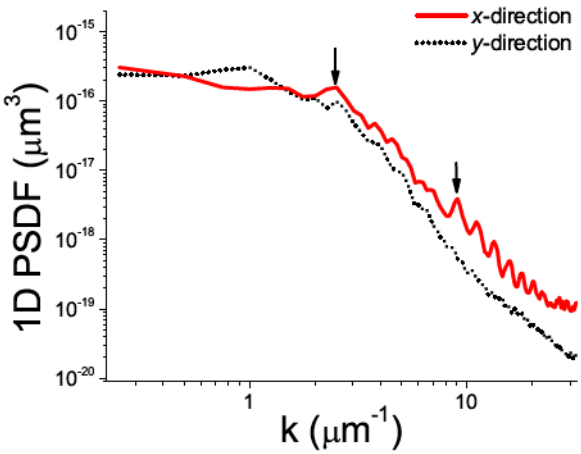

(a) $\Phi = 6.5 \times 10^{16}$ ions cm^{-2}

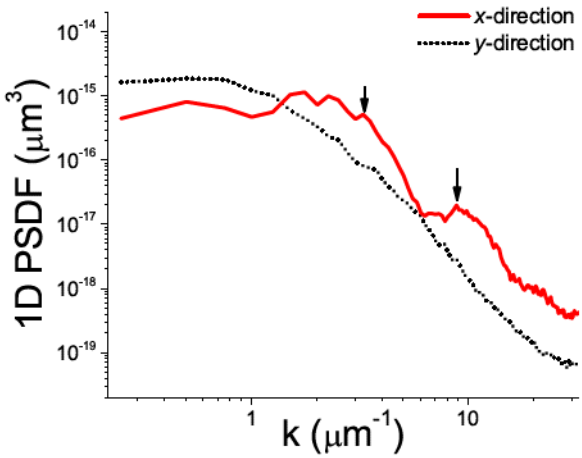

(b) $\Phi = 6.7 \times 10^{16}$ ions cm^{-2}

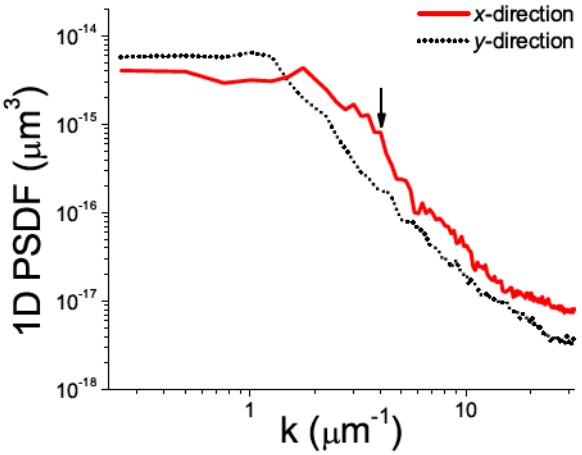

(c) $\Phi = 1.17 \times 10^{17}$ ions cm^{-2}

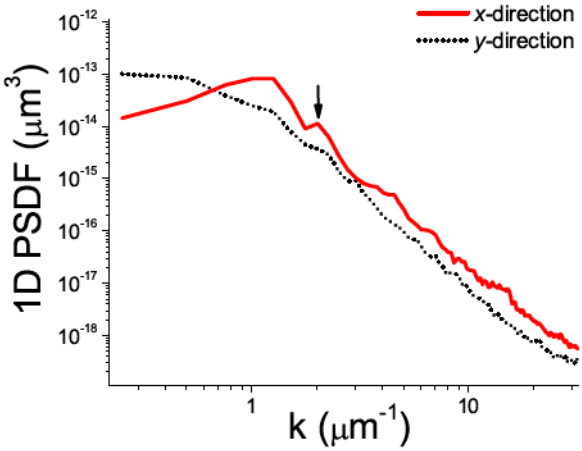

(d) $\Phi = 4.7 \times 10^{17}$ ions cm^{-2}

FIG. S3: 1D PSDF spectra for the different ion fluences in both the x and y-directions after 1.0-MeV Au ion implanted Ti at 45°angles. The ion beam direction is along the x-axis. The peaks indicated with arrows are associated to k-values for the calculated size of surface structures mentioned in the text and obtained by the relation $l_c = 2\pi/k$.

II. SURFACE BEHAVIOR WITH FLUENCE, TI-6AL-4V

The analysis of the Ti-6Al-4V ion implanted samples is similarly performed using previously defined features and statistical tools, see Figs. S4 through S6. In particular, according to PSDF and 2DACF analysis (see Fig. S7), Figure S4 a) is structureless. The height profiles confirm the absence of surface patterns (see Figure S5a), which indicates a smaller incubation fluence than for the titanium sample. For Figure S4 b), symmetric shapes have lateral sizes ≈ 0.7 μm and height ≈ 70 nm, and asymmetric shapes have lateral size ≈ 1.5 μm and height ≈ 300 nm. In Figure S4 c) the surface is populated by asymmetric shapes, as in the case of the titanium surface. Like in the Ti case, asymmetric forms are seen to connect sidewards. Cross sections of these asymmetric shapes have lateral size ≈ 1.5 μm and height ≈ 600 nm. Figure S4 d) represents a high-fluence experiment. Asymmetric structures fill the surface, with the absence of symmetric shapes. A lateral size ≈ 2.5 μm and height ≈ 1000 nm is measured.

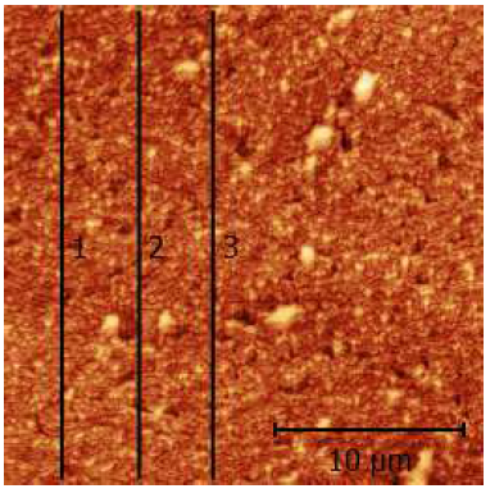

(a) $\Phi = 6.5 \times 10^{16}$ ions cm^{-2}

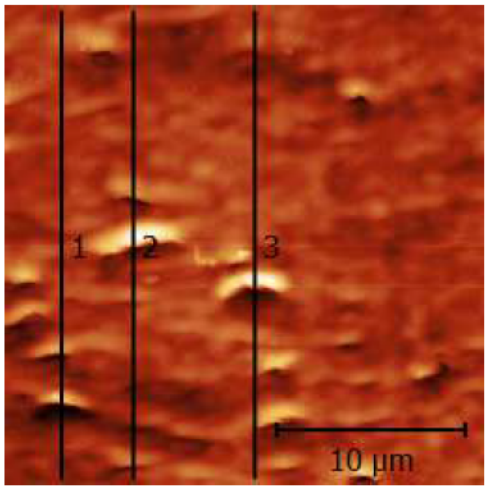

(b) $\Phi = 6.7 \times 10^{16}$ ions cm^{-2}

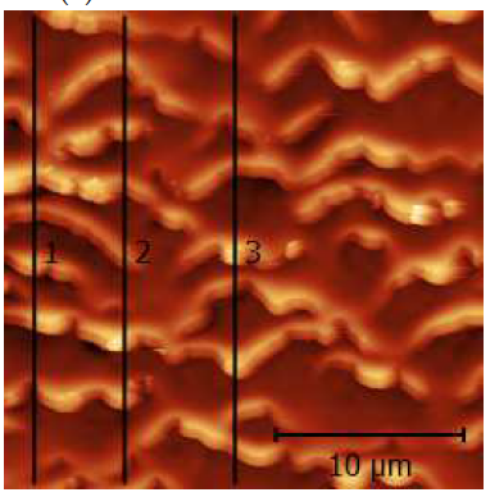

(c) $\Phi = 1.17 \times 10^{17}$ ions cm^{-2}

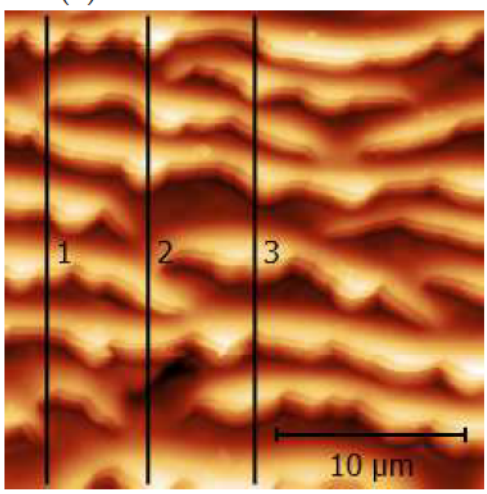

(d) $\Phi = 4.70 \times 10^{17}$ ions cm^{-2}

FIG. S4: AFM micrograph measurements of Ti-6Al-4V sputtered surfaces over 25 μm×25 μm at 45° incidence angle. The ion beam direction is from top to bottom on all images. Ion fluences are indicated in the legends. The numbered vertical solid lines on each top-view indicates the location of the corresponding line profiles shown in Fig. S5.

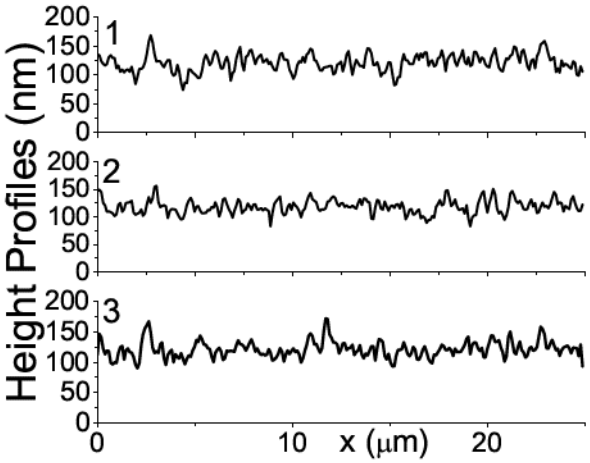

(a) $\Phi = 6.5 \times 10^{16}$ ions cm^{-2}

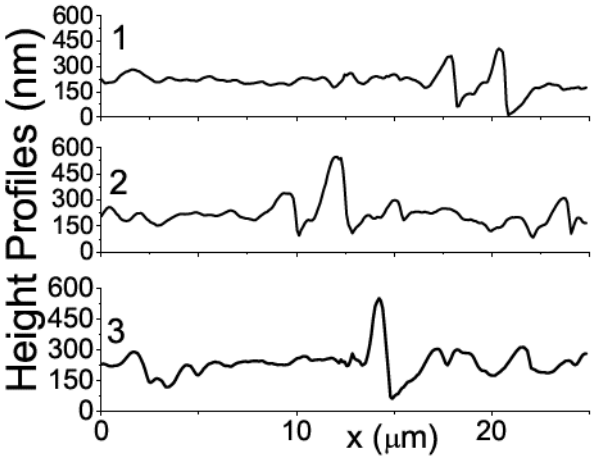

(b) $\Phi = 6.7 \times 10^{16}$ ions cm^{-2}

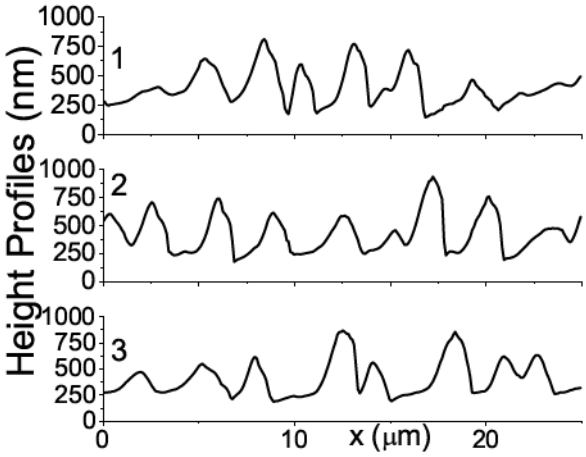

(c) $\Phi = 1.17 \times 10^{17}$ ions cm^{-2}

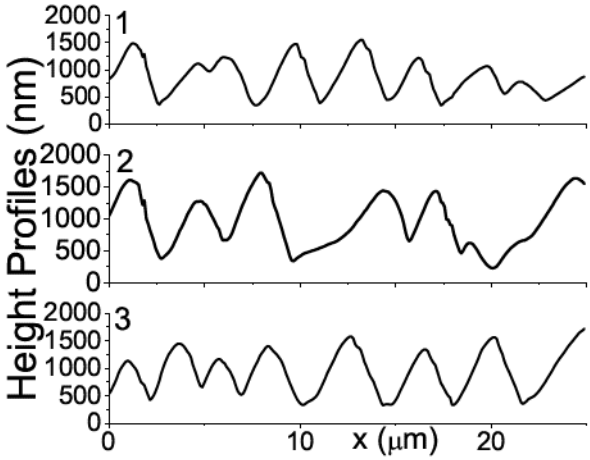

(d) $\Phi = 4.70 \times 10^{17}$ ions cm^{-2}

FIG. S5: Height profile scans of ion implanted Ti-6Al-4V surfaces at $\theta = 45°$ corresponding to the top views shown in Fig. S4. The ion beam direction is from left to right.

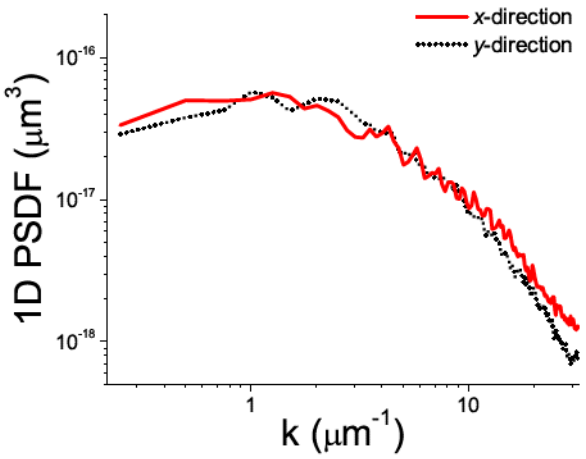

(a) $\Phi = 6.5 \times 10^{16}$ ions cm^{-2}

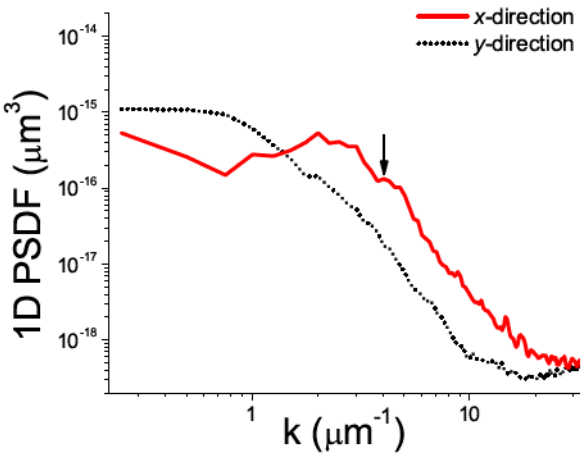

(b) $\Phi = 6.7 \times 10^{16}$ ions cm^{-2}

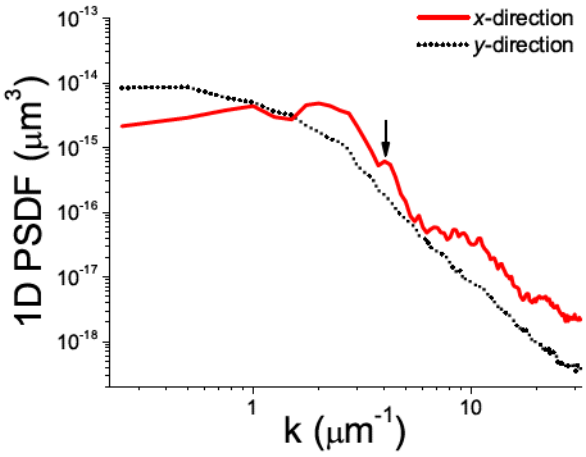

(c) $\Phi = 1.17 \times 10^{17}$ ions cm^{-2}

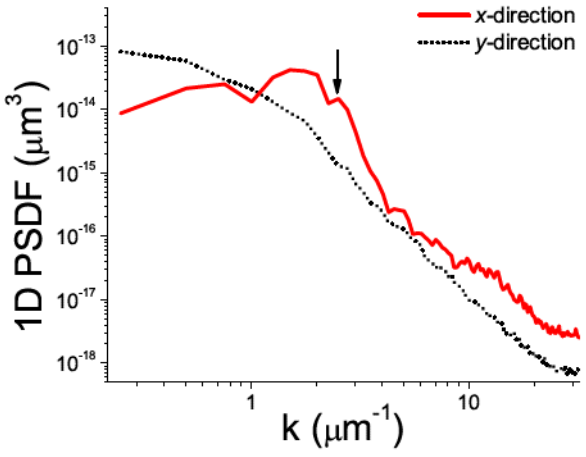

(d) $\Phi = 4.7 \times 10^{17}$ ions cm^{-2}

FIG. S6: 1D PSDF spectra for the different ion fluences in both the x and y-directions after 1.0-MeV Au ion implanted Ti-6Al-4V at 45°angles. The ion beam direction is along the x-axis. The peaks indicated with arrows are associated to k-values for the calculated size of surface structures mention in the text and obtained by the relation $l_c = 2\pi/k$.

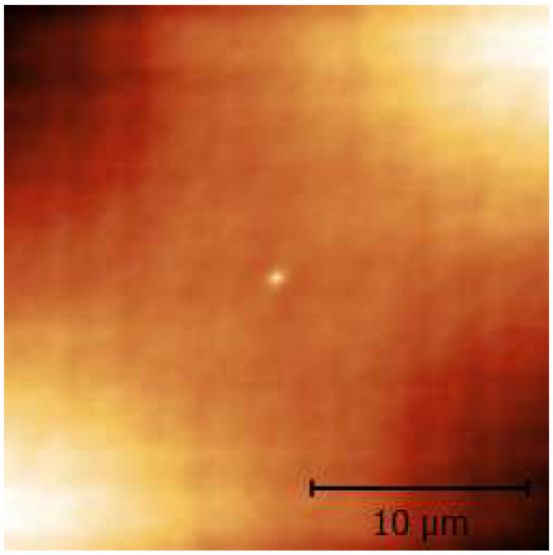

FIG. S7: 2D Auto-Correlation Function of Au ion implanted Ti-6Al-4V at $\Phi = 6.5 \times 10^{16}$ ions cm^{-2} fluence. This image indicates the lack of structure formation.

III. SURFACE BEHAVIOR WITH INCIDENCE ANGLE, TI

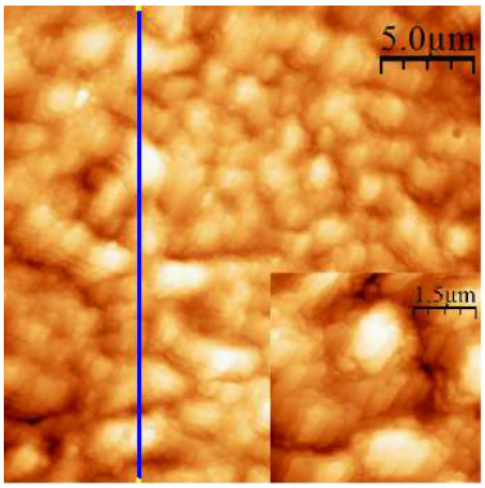

(a) $\theta = 23°$ at $\Phi = 1.68 \times 10^{17}$ ions cm^{-2}

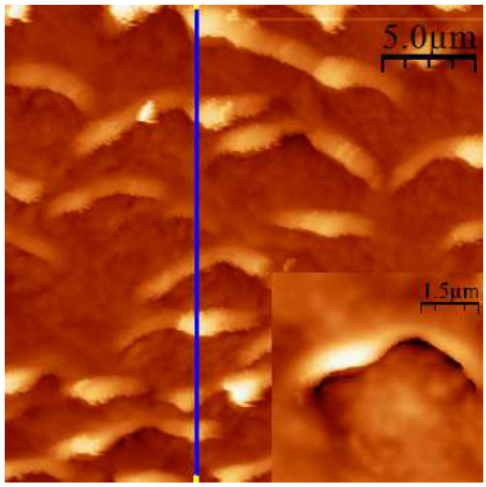

(b) $\theta = 45°$ at $\Phi = 1.17 \times 10^{17}$ ions cm^{-2}

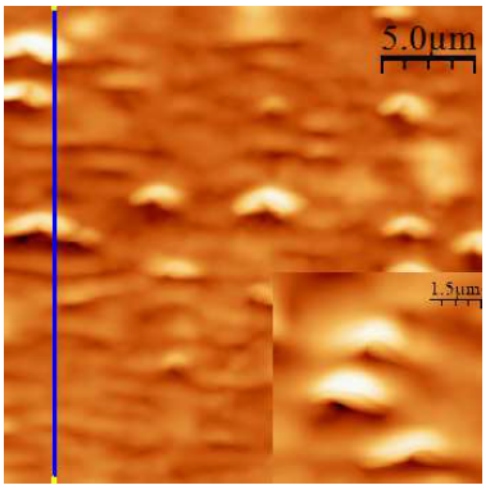

(c) $\theta = 49°$ at $\Phi = 1.33 \times 10^{17}$ ions cm^{-2}

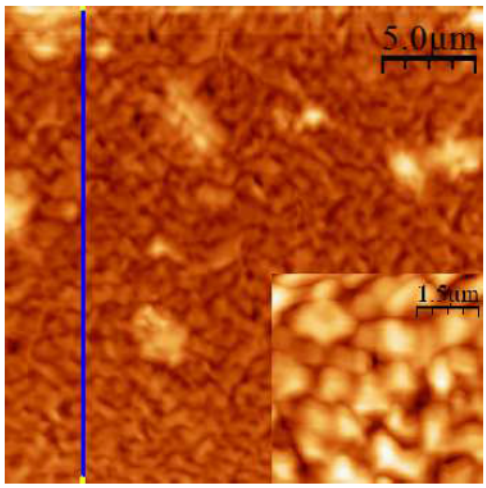

(d) $\theta = 67°$ at $\Phi = 6.70 \times 10^{16}$ ions cm^{-2}

FIG. S8: AFM micrograph measurements of Ti-sputtered surfaces over 25 μm $\times$ 25 μm (inset scale of 5 μm $\times$ 5 μm), for incidence angles and fluences as indicated in the legends. The ion beam direction of incidence is from top to bottom on all images. The vertical solid line on each top-view indicates the location of the corresponding line profile shown in Fig. 7 of the main text.

IV. SURFACE BEHAVIOR WITH INCIDENCE ANGLE, TI-6AL-4V

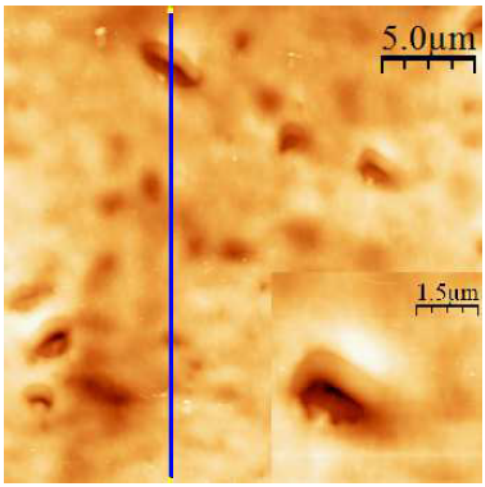

(a) $\theta = 23°$ at $\Phi = 1.68 \times 10^{17}$ ions cm^{-2}

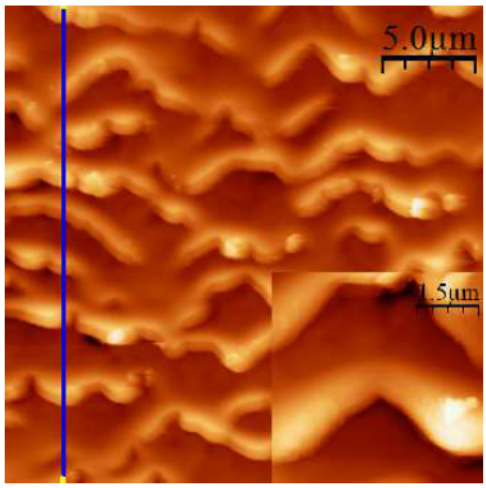

(b) $\theta = 45°$ at $\Phi = 1.17 \times 10^{17}$ ions cm^{-2}

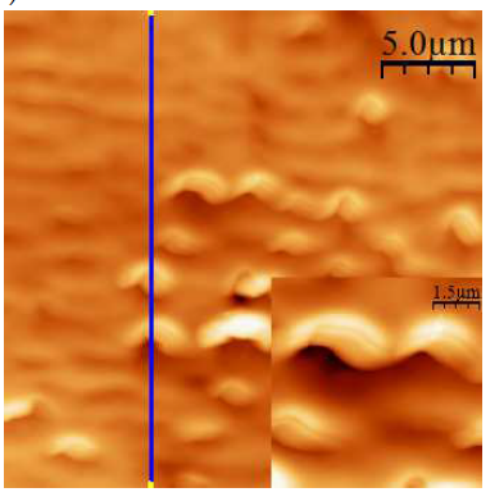

(c) $\theta = 49°$ at $\Phi = 1.33 \times 10^{17}$ ions cm^{-2}

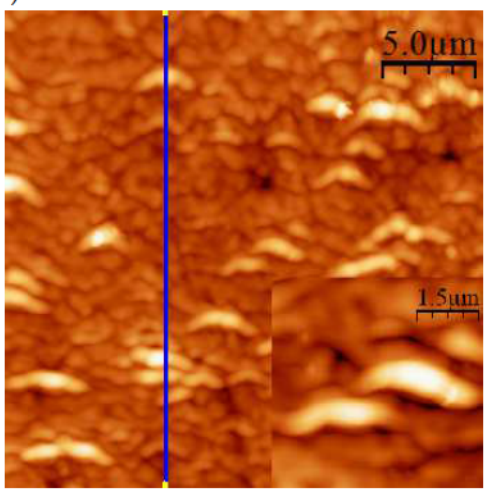

(d) $\theta = 67°$ at $\Phi = 6.70 \times 10^{16}$ ions cm^{-2}

FIG. S9: AFM micrograph measurements of Ti-6Al-4V sputtered surfaces over 25 μm × 25 μm (inset scale of 5 μm × 5 μm), for incidence angles and fluences as indicated in the legends (compare also with Fig. S8). The ion beam direction of incidence is from top to bottom on all images. The vertical solid line on each top-view indicates the location of the corresponding line profile shown in Fig. 7 of the main text.

V. RESULTS FROM SRIM SIMULATIONS

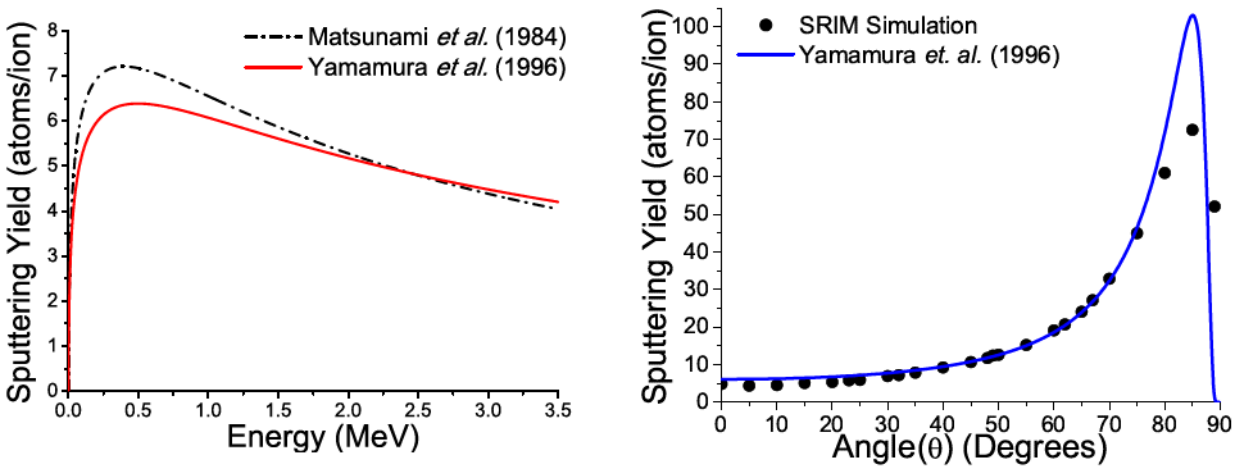

FIG. S10: Energy (left, for $\theta = 0°$) and angle of incidence (right, for $E = 1$ MeV) dependence of the sputtering yield for Au ion implantation of Ti. Semiempirical models of the sputtering yield [1, 2] have been considered.

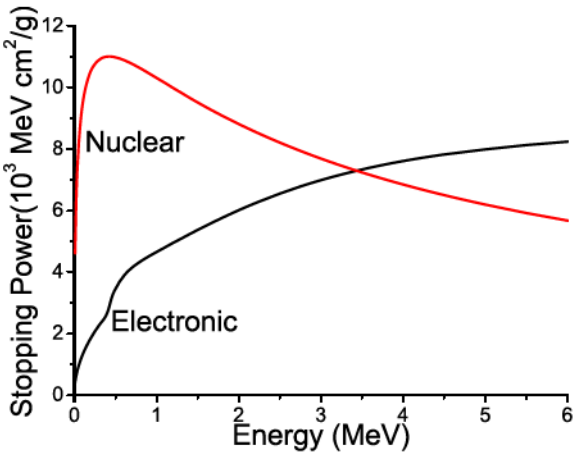

FIG. S11: Energy dependence of the electronic and nuclear stopping power for Au ions in Ti.

REFERENCES

[1] N. Matsunami, Y. Yamamura, N. Itikawa, Y. Kazumata, S. Miyagawa, K. Morita, R. Shimizu, and H. Tawara, *Energy dependence of the ion-induced sputtering yields of monatomic solids* At. Data Nucl. Data Tables **31**, 1 (1984).

[2] Y. Yamamura and H. Tawara, *Energy dependence of ion-induced sputtering yields from monatomic solids at normal incidence* At. Data Nucl. Data Tables **62**, 149 (1996).